

Large Eddy Simulations of Turbulent Pipe Flows at Moderate Reynolds Numbers

Himani Garg,¹ Lei Wang,¹ Martin Andersson,¹ and Christer Fureby¹

¹Lund University, Department of Energy Sciences, P.O. Box 118, SE-22100 Lund, Sweden

(*Electronic mail: himani.garg@energy.lth.se; himani.garg65@gmail.com)

ABSTRACT

Wall-bounded turbulence is relevant for many engineering and natural science applications, yet there are still aspects of its underlying physics that are not fully understood, particularly at high Reynolds numbers. In this study, we investigate fully-developed turbulent pipe flows at moderate-to-high friction velocity Reynolds numbers ($361 \leq Re_\tau \leq 2,000$), corresponding to bulk velocity-based Reynolds numbers of $11,700 \leq Re_b \leq 82,500$, using wall-modeled Large Eddy Simulations (LES) in OpenFOAM. A grid convergence study is performed for $Re_\tau = 361$, followed by an investigation of the accuracy of various subgrid-scale stress models for the same Reynolds number. Results show that the Wall-Adapting Local Eddy (WALE) model performs well compared to experiments and Direct Numerical Simulations (DNS), while One-Equation Eddy-Viscosity Model (OEEVM) and Smagorinsky (SMG) are too dissipative. LES utilizing WALE are then performed for four different Reynolds numbers with gradually refined grids, revealing excellent agreement with DNS data in the outer region. However, a significant deviation from DNS data is observed in the sub-viscous layer region, indicating the need for further mesh refinement in the wall-normal direction to accurately capture the smallest-scale motions' behavior. Additional mesh sensitivity analysis uncovered that, as the Re_τ value rises, it becomes crucial for a grid to adhere to the condition of $\Delta x^+ \leq 20 - 25$ and $\Delta z^+ \leq 10$ in order to precisely capture substantial large and small scale fluctuations. Overall, the WALE model enables accurate numerical simulations of high-Reynolds-number, wall-bounded flows at a fraction of the computational cost required for temporal and spatial resolution of the inner layer.

Keywords: Large eddy simulations, Wall-bounded-turbulence, statistical analysis

I. INTRODUCTION

Two common features of engineering and environmental fluid flows are wall-boundedness [1, 2] and high Reynolds number (Re) turbulence [3–5]. The study of turbulent flow traces back over a century, and its widespread application has kept this field under constant development [6]. The spatially evolving boundary layer, the channel, and the pipe are three canonical building block flows for wall bounded turbulent flows. Consequently, pipe flow is fully described by Re and the length of the pipe. The effect of the pipe length is insignificant only if considered sufficiently large [7]. During the transport of fluids through pipes, roughly half of the energy is dissipated by turbulence near the walls [8]. The need to investigate fundamental wall-bounded turbulence at high Re is widely agreed in literature. Clauser [9] and Coles & Hirst [10] provided a comprehensive review of classical wall-bounded turbulent scaling and structure for the case of a smooth wall. However, one of the most recent revealing research result comes from efforts seeking to achieve an ever-higher Re number and, in doing so, shedding light on some of the longstanding questions about the very nature of wall-bounded turbulence, including how well our present analytical and computational models match its complex behavior [3].

To date, accurate high- Re -number data are still primarily achievable only via well-designed experiments [11]. With the progress of computational technology, simulations have emerged to play a vital role in research on turbulent flows and wall-bounded turbulence. One of the most cited articles on turbulent pipe flow is by Eggels *et al.* [12], showing compar-

isons between Direct Numerical Simulation (DNS) and experimental results of Hot Wire Anemometry, Particle Image Velocimetry, and Laser Doppler Anemometry at nominally similar friction-velocity-based turbulent $Re_\tau = u_\tau h / \nu \simeq 180$, where u_τ the friction velocity, h the characteristic length, and ν the kinematic viscosity. Numerous studies (e.g., [13–16]) have extensively documented the effects at low Re_τ . These studies illustrate the augmentation in the maxima of stream-wise turbulence intensity and Reynolds shear stress, along with inner-scaled turbulence statistics correlated with Re_τ . These effects are predominantly observed in the logarithmic law of the mean velocity profiles, attributed to higher pressure gradients. Nevertheless, decades of experimental research have shown that obtaining detailed high- Re_τ data, notably near the wall, remains challenging. That is because as Re_τ increases, the smallest length scales decrease, and as a result lead to significant uncertainties in determining the probe locations and turbulence intensities. Recently, DNS of turbulent pipe flows with Re_τ ranging from 500 to 6,000 have been presented [7, 17–24]. These Re_τ are considered modest compared to turbulent pipe flow experiments carried out with a turbulent Re range of $Re_\tau \simeq O(10^3 - 10^5)$ [11, 25–28].

As Re_τ increases, the range of turbulent scales extends, demanding higher resolutions for DNS. However, the number of required grid points for DNS scales roughly as $O(Re_\tau^{9/4})$ [29], presently falling short of computing capability at engineering Re_τ values. Capturing the turbulent flow and accounting for additional computing overhead requires computer resources that scale nominally as Re_τ^4 [30]. Considering that many real-world flows have $Re_\tau > 10^6$, the computing costs associated with DNS quickly becomes prohibitive.

On the other hand Large Eddy Simulations (LES) takes a different approach, by filtering of the smallest scales and replacing their effects on the large resolved scales by subgrid models [31]. LES of unbounded homogeneous and shear turbulence is well established [32–35], whereas LES of wall-bounded flows has remained challenging, firstly, because the presence of a wall causes the length scales to progressively decrease toward the wall, and secondly, owing to the near-wall anisotropy.

When a wall is present the LES grid is typically constrained by the near-wall region, where turbulent and viscous momentum transport occur on small scales. Piomelli & Balars [36] showed that for near-wall-resolved LES, around 99% of grid points are used to resolve the wall layers in fully-developed channel flow. As a result, for wall-bounded flows the computational cost of near-wall-resolved LES to resolve the viscous sublayer is estimated to scale as $Re_\tau^{1.8}$, which demonstrates the potential savings over DNS [36]. Nevertheless, the development of wall-modeled LES [36–40] has widened the range of applications of LES for wall-bounded flows. In near-wall-modeled LES, the effects of the near-wall anisotropic fine scales are not resolved but modeled by wall models, approximating the near-wall physics. Near-wall-modeled LES is computationally more efficient than near-wall-resolved LES since only the outer layer is explicitly computed, with the required grid size determined by the outer flow eddies [36, 41–44]. Thus in wall-modeled LES, the grid requirements could be relaxed; it is estimated that the computational costs would scale as $Re_\tau^{0.2}$ [45]. Sagaut [31] gives a thorough description of the (still on-going) efforts in the formulation of more accurate LES models. Yet few simulations have been performed at high Re .

To the best of our knowledge, the highest turbulent Re_τ used in LES of turbulent pipe flows were $Re_\tau \simeq 2,000$ and 180,000, by Berrouk *et al.* [46] and Ferrer *et al.* [47]. The authors present explicit and implicit LES of fully-developed turbulent pipe flows using a continuous Galerkin spectral element solver, motivated by the work of Chung & Pullin [40]. For explicit LES they utilized the explicit stretched-vortex model of Chung & Pullin [40]. From the literature review, it is evident that only a limited number of studies have been conducted with wall-modeled LES focusing on the moderate-to-high Re_τ wall-bounded turbulent flow. The objective of the present study is to carry out wall-modeled LES for moderate to high Re_τ and compare the results to DNS at matched Re_τ for internal wall-bounded flows. To perform wall-modeled LES, different meshes have been generated, with y^+ values from 4 to 11. We study the performance of different subgrid models, investing their accuracy at predicting the statistical behavior of moderate Re fully-developed turbulent pipe flows. Five subgrid models are considered: the Wall-Adapting Local Eddy viscosity model (WALE) [48], the Smagorinsky model (SMG) [49], the One-Equation Eddy Viscosity Model (OEEVM) [50], the Localized Dynamic Kinetic energy Model (LDKM) [51, 52], and the Differential Stress Equation Model (DSEM) [53]. Only the WALE model is selected to investigate the dependence on grid resolution, as a trade-off between computational cost and numerical accuracy. For detailed investigation, four friction-velocity-

based turbulent Re are considered: $Re_\tau = 361, 550, 1,000,$ and $2,000$. The simulations are evaluated based on predictions of zeroth-, first-, and second-order turbulence statistics and flow features such as friction coefficient, mean velocity profiles, velocity correlations, mean turbulent shear stress profiles, quadrant analysis, and anisotropy invariant maps. Numerical results for each model are compared with DNS data [7, 23].

II. LES METHODOLOGY

A. Mathematical formulation

In LES, the governing equations are the low pass filtered conservation equations of incompressible flow mass and momentum as represented by,

$$\frac{\partial \bar{u}_i}{\partial x_i} = 0, \quad (1)$$

$$\frac{\partial \bar{u}_i}{\partial t} + \frac{\partial}{\partial x_j} (\bar{u}_i \bar{u}_j) = -\frac{1}{\rho} \frac{\partial \bar{p}}{\partial x_i} - \frac{\partial \tau_{ij}^{sgs}}{\partial x_j} + \frac{\partial}{\partial x_j} \left(\nu \frac{\partial \bar{u}_i}{\partial x_j} \right), \quad (2)$$

where \bar{u}_i is the filtered velocity, \bar{p} , the filtered pressure, ν , the kinematic viscosity, and $\tau_{ij}^{sgs} = \bar{u}_i \bar{u}_j - \bar{u}_i \bar{u}_j$, the subgrid stress tensor. Mathematical analysis and physical arguments, e.g., [54–56], suggest that: (i) τ_{ij}^{sgs} is invariant under a change of frame; (ii) τ_{ij}^{sgs} is positive-definite symmetric, provided that the filter function, G_Δ , is symmetric; and (iii) the inequalities $k = \frac{1}{2} \text{tr}(\tau_{ij}^{sgs}) \geq 0$, $k^2 \geq \left\| \tau_{ij}^{sgs} \right\|^2$, and $\det(\tau_{ij}^{sgs}) \geq 0$ must be satisfied for τ_{ij}^{sgs} to be positive-definite.

B. Subgrid modeling

Two methodologies are usually adopted for subgrid modeling: functional modeling, which consists in modeling the action of the subgrid scales on the resolved scales, and structural modeling, whose principle is to model the subgrid stresses without incorporating any knowledge about the interactions between the subgrid and resolved scales [31]. However, for the purpose of this paper, we instead prefer to focus on isotropic and anisotropic subgrid models since complex flows with high Re numbers are often characterized by anisotropy on a wide range of scales – typically reaching the range of scales that require modeling, e.g., in the near-wall region. The most frequently used subgrid models are the eddy-viscosity models. This type of models computes the deviatoric part of the subgrid stress tensor by relating it, in a linear correspondence, to the rate-of-strain tensor, $S_{ij} = \frac{1}{2}(\partial u_i / \partial x_j + \partial u_j / \partial x_i)$ [57]. By doing so, the subgrid stress tensor may be thought of being decomposed into an isotropic part and an anisotropic part. The former is also known as the normal stresses and is directly related to the turbulent kinetic energy while the latter measures the deviations from isotropy. Hence, the subgrid stress tensor, based

on the Boussinesq hypothesis, is expressed as

$$\tau_{ij}^{\text{sgs}} - \frac{2}{3}k_{\text{sgs}}\delta_{ij} = -2\nu_{\text{sgs}}\bar{S}_{ij}, \quad (3)$$

where ν_{sgs} is the subgrid eddy viscosity and δ_{ij} is the Kronecker delta. Models for the eddy viscosity, ν_{sgs} , and the subgrid turbulent kinetic energy, $k_{\text{sgs}} = \frac{1}{2}\text{tr}(\tau_{ii}^{\text{sgs}})$, are needed to close Eq. (3). For this purpose, we assume the existence of characteristic length and velocity scales and we infer separation between the resolved and subgrid scales.

In this work, we limit ourselves to five well-known LES subgrid models: Firstly, the One-Equation Eddy Viscosity Model (OEEVM) [50], in which a modeled transport equation for k_{sgs} is solved, and $\nu_{\text{sgs}} = c_k\Delta k_{\text{sgs}}^{1/2}$ is modeled, where $c_k = 0.094$ and $c_\varepsilon = 1.048$.

The second model is the Smagorinsky (SMG) model [49] which assumes a local equilibrium between production and dissipation of k_{sgs} . As a result, the subgrid viscosity and kinetic energy becomes, $\nu_{\text{sgs}} = c_s^2\Delta^2(2\bar{S}_{ij}\bar{S}_{ij})^{1/2}$ and $k_{\text{sgs}} = c_l\Delta^2(2\bar{S}_{ij}\bar{S}_{ij})$, where $c_k = 0.094$, $c_\varepsilon = 1.048$, $c_l = c_k/c_\varepsilon = 0.089$, and $c_s = c_k\sqrt{c_k/c_\varepsilon}$ are the model coefficients [49, 58].

The third model is the Localized Dynamic Kinetic energy Model (LDKM) based on the work of Kim and Menon [51, 52]. In the LDKM, scale similarity between the subgrid-scale stress tensor and the test-scale Leonard stress tensor is assumed to evaluate the model coefficients, for ν_{sgs} and the subgrid dissipation, ε . The transport equation used in this model is similar to that in OEEVM model. The expression for ν_{sgs} is similar to the one of the OEEVM model: $\nu_{\text{sgs}} = c_k\Delta k_{\text{sgs}}^{1/2}$, except that the model coefficient, c_k , is now evaluated dynamically as $c_k = \frac{1}{2}\frac{L_{ij}M_{ij}}{M_{ij}M_{ij}}$, where $M_{ij} = -\tilde{\Delta}\mathbf{K}^{1/2}\tilde{\tilde{S}}_{ij}$,

$L_{ij} = \widetilde{\widetilde{u_i u_j}} - \widetilde{\widetilde{u_i}}\widetilde{\widetilde{u_j}}$, $\mathbf{K} = \frac{1}{2}L_{ii}$, and the tilde symbol, $\widetilde{(\cdot)}$, denotes the explicit filtering operation, usually defined as twice the original filter, e.g., $\tilde{\Delta} = 2\Delta$. The subgrid dissipation is modeled as $\varepsilon \approx c_\varepsilon\mathbf{K}^{3/2}/\tilde{\Delta}$ in which c_ε is evaluated dynamically as $c_\varepsilon = \frac{\widetilde{\widetilde{g_{ij}g_{ij}} - \widetilde{\widetilde{g_{ij}}}\widetilde{\widetilde{g_{ij}}}}}{[(\nu + \nu_{\text{sgs}})\tilde{\Delta}]^{-1}\mathbf{K}^{3/2}}$, with $\bar{g}_{ij} = \partial\bar{u}_i/\partial x_j$ being the filtered velocity gradient.

The fourth model is the Wall-Adapting Local Eddy viscosity (WALE) model [48]. This method allows to obtain a subgrid viscosity proportional to the wall-normal distance cubed ($\nu_{\text{sgs}} \propto y^3$), and additionally allows the subgrid viscosity to vanish near the solid walls. The WALE model can be defined via the following relation for subgrid viscosity, $\nu_{\text{sgs}} = c_w\Delta^2 \frac{(S_{ij}^d S_{ij}^d)^{3/2}}{(\bar{S}_{ij}\bar{S}_{ij})^{5/2} + (S_{ij}^d S_{ij}^d)^{5/4}}$, where $S_{ij}^d = \frac{1}{2}(\bar{g}_{ij}^2 + \bar{g}_{ji}^2) - \frac{1}{3}\delta_{ij}\bar{g}_{ij}^2$ is the traceless symmetric part of the square of the velocity gradient tensor.

Lastly, we consider the Differential Stress Equation Model (DSEM) by Deardorff [53], which does not rely on the local isotropy assumption within the subgrid scales. The DSEM employed here uses a modeled transport equation for the sub-

grid stress tensor, τ_{ij} , following [53],

$$\begin{aligned} \frac{\partial \tau_{ij}^{\text{sgs}}}{\partial t} = & -\frac{\partial}{\partial x_k}(\tau_{ij}^{\text{sgs}}\bar{u}_k) - \tau_{ik}^{\text{sgs}}\frac{\partial \bar{u}_j}{\partial x_k} - \tau_{jk}^{\text{sgs}}\frac{\partial \bar{u}_i}{\partial x_k} \\ & - \frac{\partial}{\partial x_k}\overline{u'_i u'_j u'_k} + p'\left(\frac{\partial u'_i}{\partial x_j} + \frac{\partial u'_j}{\partial x_i}\right) - 2\nu\frac{\partial u'_i}{\partial x_k}\frac{\partial u'_j}{\partial x_k}. \end{aligned} \quad (4)$$

The fourth, fifth, and sixth terms on the right-hand side of Eq. 4, which represent triple correlation, pressure-strain correlation, and the dissipation term, are modeled, and details can be found in [31, 59].

The van Driest wall-damping function is used in the wall treatment for the SMG and OEEVM subgrid models. Whereas, a wall-model is instead used for the WALE, DSEM, and LDKM models. This wall model is based on the Spalding's law of the wall from which the friction velocity can be estimated based on which a wall viscosity can be derived at the first off-wall grid point, following the ideas of [41].

III. SIMULATION DETAILS

The LES equations are solved numerically using the finite volume method with a second-order cell-centered discretization scheme using OpenFOAM. Time stepping is performed using the second-order accurate implicit Adams-Bashforth method [60] with a maximum Courant-Friedrichs-Lewy (CFL) number of 0.5 for numerical stability. The PISO algorithm for LES is used to decouple the pressure-momentum equations [61]. The resulting pressure equation is solved using a Generalized Geometric-Algebraic Multigrid (GAMG) method with a Diagonal Incomplete Cholesky (DIC) smoother [62]. Velocity, turbulent kinetic energy, and dissipation rate are solved using a Preconditioned BiConjugate Gradient (PBiCG) solver [63] with a Diagonal Incomplete Lower-Upper (DILU) preconditioning method [62].

The turbulent bulk Re_b number based on the pipe diameter, D , and bulk velocity, U_b , is given by

$$Re_b = \frac{U_b D}{\nu}, \quad (5)$$

yielding the four values $Re_b = 11,700, 19,000, 37,700,$ and $82,500$ used in this study. The motivation behind selecting these Re_b values is the well-established DNS results previously reported [7, 23]. To provide a direct comparison of LES results with DNS, we use the same values of Re_b as reported in these papers. In addition to the bulk velocity, another characteristic velocity scale is commonly introduced in connection with wall-bounded flows. The friction velocity, u_τ , is defined in terms of the wall shear stress, τ_w , and the fluid density, ρ , as

$$u_\tau = \sqrt{\frac{\tau_w}{\rho}}. \quad (6)$$

The turbulent friction Re_τ number, based on the pipe radius, R , and friction velocity, u_τ , is given by

$$Re_\tau = \frac{u_\tau R}{\nu}, \quad (7)$$

yielding the four values $Re_\tau = 361, 550, 1,000,$ and $2,000$ used in this study.

Hexahedral butterfly grids, have been used for all simulations. These grids are composed of a Cartesian part at the center of the pipe surrounded by four transitional regions from the inner square to the outer circle of all cross-sections of the pipe. Such grids thus require the definition of a partition of the pipe into five blocks prior to the grid generation, but generally provide the best grid quality, i.e., high orthogonality and low grid density. The generation of these grids is automated by means of an m4 macro [64] in OpenFOAM. The length of the computational domain is L . The radial, axial, and azimuthal directions are represented by $r, x,$ and θ , and the corresponding velocity components, by $u, v,$ and w . The wall-normal distance, i.e., along the radial direction, is denoted by $y = R - r$, where $R = D/2$ is the pipe radius. Here, $u', v',$ and w' are the velocity fluctuations in the streamwise, radial, and azimuthal directions, respectively.

Since the fully-developed turbulent pipe flow considered here is homogeneous in the streamwise direction, periodic boundary conditions are imposed in this direction. No-slip boundary conditions are imposed at the pipe wall for all velocity components, whereas zero-Neumann boundary condition is used for the pressure. An additional external force term is introduced into the NSE to mimic the effect of the pressure gradient in the context of periodic boundary conditions in the streamwise direction. The magnitude of this force is determined by the bulk velocity. For the present study we chose the pipe length to be five times the pipe diameter, i.e., $L = 10R$. Indeed, to ensure that statistics are not affected by the streamwise periodic boundary conditions, we have investigated one-dimensional temporal and spatial autocorrelation functions of velocity fluctuations. The results are presented in Appendix B and show that the chosen domain length is sufficiently large for velocity fluctuations to uncorrelate. All flow statistics are averaged over approximately 100 to 120 flow-through times.

IV. RESULTS AND DISCUSSIONS

This discussion is mainly subdivided into three main sections. In Sec. IV A simulations for statistically fully-developed turbulent pipe flow at $Re_\tau = 361$ are presented. These simulations correspond to four different mesh resolutions. The results are grouped according to the computed quantities, e.g., mean flow profiles, Reynolds shear stresses, and friction factor. In Sec. IV B fully-developed turbulent pipe flow simulations at fixed $Re_\tau = 361$, for five LES models are performed. In Sec. IV C LES-WALE simulations for four moderate-to-high turbulent Re_τ are carried out. Again, in both sections results are grouped based on the computed quantities.

A. Mesh independence study of fully-developed turbulent pipe flows

LES-WALE simulations for pipe flows are performed at $Re_\tau = 361$ used four different meshes, named M1, M2, M3, and M4, with cell counts varying from 0.13 to 5 million. Table I provides details about these meshes, such as total cell count, cells along the flow direction, maximum skewness and aspect ratio, and Δy^+ ranges.

Figure 1 shows the resulting flow using isosurfaces of the second invariant of the velocity gradient tensor, λ_2 [65], obtained through the LES-WALE simulations at different mesh resolutions. Vortices are identified using the λ_2 -criterion and presented for $\lambda_2/\lambda_{2\max} = -0.01$, where more negative values indicate stronger vortices. The pipe shows a dense collection of turbulent eddies from the wall up to $y/R \simeq 0.5$. Coarser grids (M1 and M2) exhibit fewer vortical structures in the boundary layers, forming elongated axial vortices with length scales around $0.1R$. Higher mesh resolution helps capture finer structures near the wall, reducing numerical dissipation. Despite differences in mesh, fluctuations appear similar from M1 to M4. Meshes M3 and M4 show similar turbulence statistics, suggesting convergence and independence from mesh sensitivity.

In Fig. 2, (a) shows mean velocity profiles in inner variables for four grid resolutions and includes DNS data from El Khoury *et al.* [7] in a pipe flow. The profiles are computed along a vertical line through the pipe center. Higher mesh resolution causes a downward shift in the overlap region compared to DNS data. Although there is a slight difference in the inner layer for M1, the profiles maintain a similar shape across different mesh resolutions. Unlike turbulent channel flows in experiments or numerical simulations [66–69], the mean velocity profiles do not align with the logarithmic velocity distribution, $\langle u \rangle^+ = (1/\kappa) \log(y^+) + B^+$ for $y^+ > 200$, where $\kappa = 0.4$ is the Von Kármán constant and $B^+ = 5.2$. This discrepancy is likely due to a wake region near the pipe centerline [7]. Additionally, (b) tests the law of the wall by plotting mean profiles in velocity-deficit form in Fig. 2. Differences in mesh resolution become more evident. Transitioning from M1 to M4, profiles shift toward DNS data, and excellent overall agreement with DNS is achieved for M3 and M4.

Figure 3 assesses mesh sensitivity by presenting streamwise, wall-normal, and azimuthal root-mean-squared velocity profiles against the wall distance with inner scaling. As mesh resolution increases, results progressively align with DNS data (dashed black line). Notably, M1 and M2 show different flow behavior in the outer layer ($y^+ > 50$) compared to M3 and M4. The finest grid yields excellent agreement with DNS across the entire region, while M3 and M4 produce similar results despite their resolution difference, indicating statistical independence for these two grids. The positive impact of grid refinement is evident in the gradual increase in result accuracy. Additionally, root-mean-squared velocity fluctuations, $u_{\text{rms}}^+, v_{\text{rms}}^+,$ and w_{rms}^+ , converge toward DNS results with grid refinement. The peak value of u_{rms}^+ consistently occurs at $y^+ \simeq 15$, observed in various studies across wall-bounded flows. In Fig. 3 (d), pro-

TABLE I: Mesh properties.

Mesh	Ncells along x -direction	Total size	Δy^+	Maximum skewness	Maximum aspect ratio
M1	80	122,640	4.50	0.59	7.46
M2	120	430,080	3.60	0.61	7.86
M3	180	1,451,520	2.35	0.62	7.83
M4	270	4,898,880	1.65	0.63	7.81

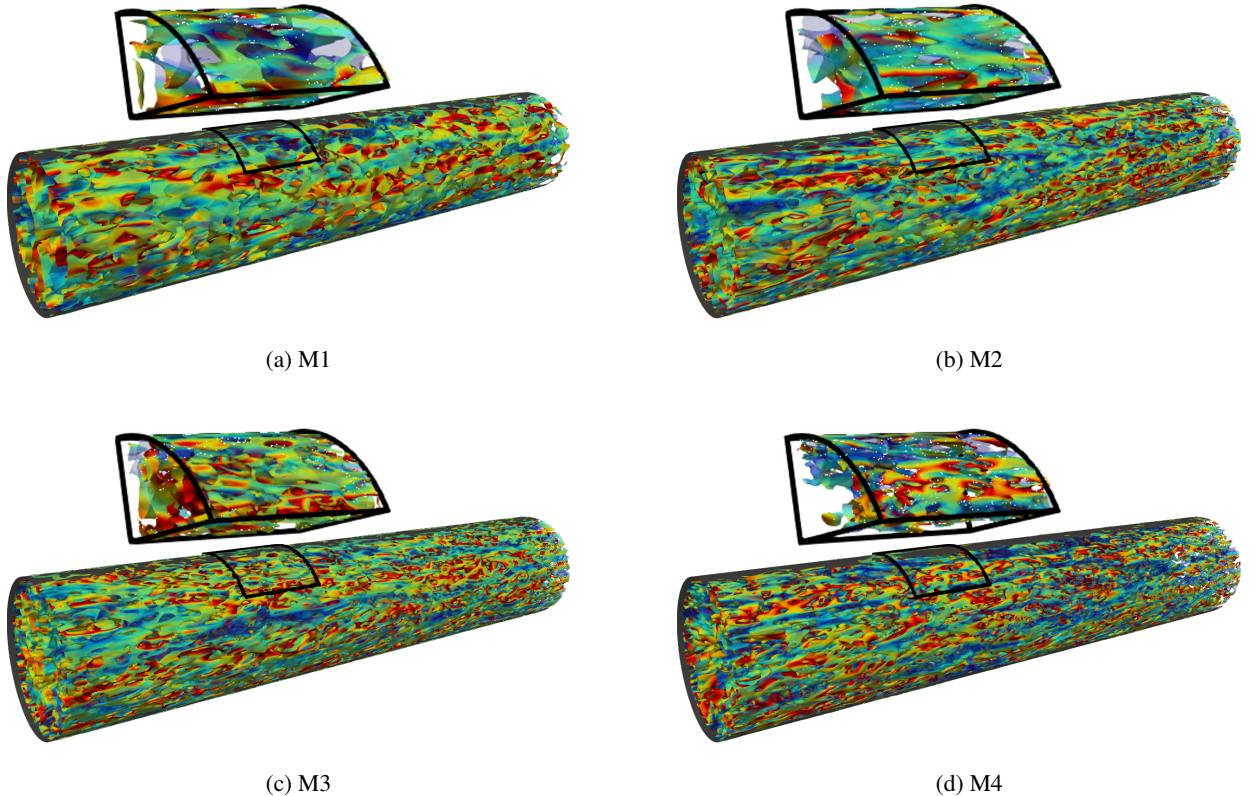


FIG. 1: Visualization of vortical structures using the λ_2 -criterion, colored with streamwise velocity fluctuations, u' , at $Re_\tau = 361$ for (a) M1, (b) M2, (c) M3, and (d) M4. Color scale ranges from -0.3 (blue) to 0.3 (red) and zoomed-in views are provided for clarity.

files of Reynolds shear stress, crucial for momentum transport in wall-bounded turbulence, are presented. Reynolds shear stress near the wall is scaled by classic inner scaling as u_τ^2 [70]. Regardless of mesh resolution, all profiles collapse well for $y^+ \leq 16$ and scale as u_τ^2 . As mesh resolution increases, results increasingly agree with DNS data (dashed black line). M3 and M4 stand out, providing exceptionally good results, while M1, being a very coarse mesh, leads to the underprediction of most turbulent properties.

To conclude the mesh sensitivity study, friction factor (f_D) values are calculated using $f_D = 8\tau_w/(\rho \langle u \rangle^2)$ [71] for each simulation and compared with values from the Colebrook correlation [72] in Table II. In all cases, f_D values are slightly underpredicted compared to empirical formulations, as expected due to the nature of turbulence models used in LES, which do not fully resolve wall dynamics. However, with a

gradual increase in grid resolution and refinement near the wall, the results improve noticeably. The relative error in the friction coefficient, $f_{D_{\text{relErr}}} = |f_{D_{\text{num}}} - f_{D_{\text{exp}}}|/f_{D_{\text{exp}}} \times 100\%$, tends towards zero. Once again, the measurement of f_D shows that M3 and M4 exhibit similar behavior and outperform other grids in terms of accuracy.

B. Different subgrid model behavior for $Re_\tau = 361$

To evaluate the predictive capabilities of the subgrid models, numerical simulations of a turbulent pipe flow at a fixed turbulent $Re_\tau = 361$, are performed, comparing results against previously reported DNS findings [7]. This comparison involves five different subgrid models (SMG, OEEVM, WALE, LDKM, and DSEM). As we refine the mesh resolu-

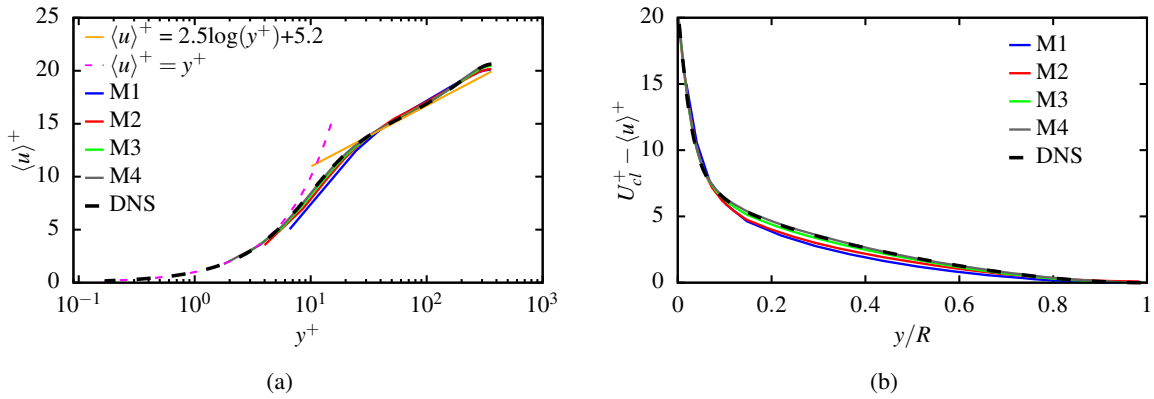


FIG. 2: Comparison of LES-WALE and DNS data for mean velocity profiles (a) in inner variables and (b) in velocity-defect form. U_{cl}^+ is the normalized centerline velocity. DNS data at $Re_\tau = 361$ is shown in dashed black line. The dashed-dotted pink and solid orange lines in Fig. 2 (a) represent the universal behavior of the turbulent velocity profile.

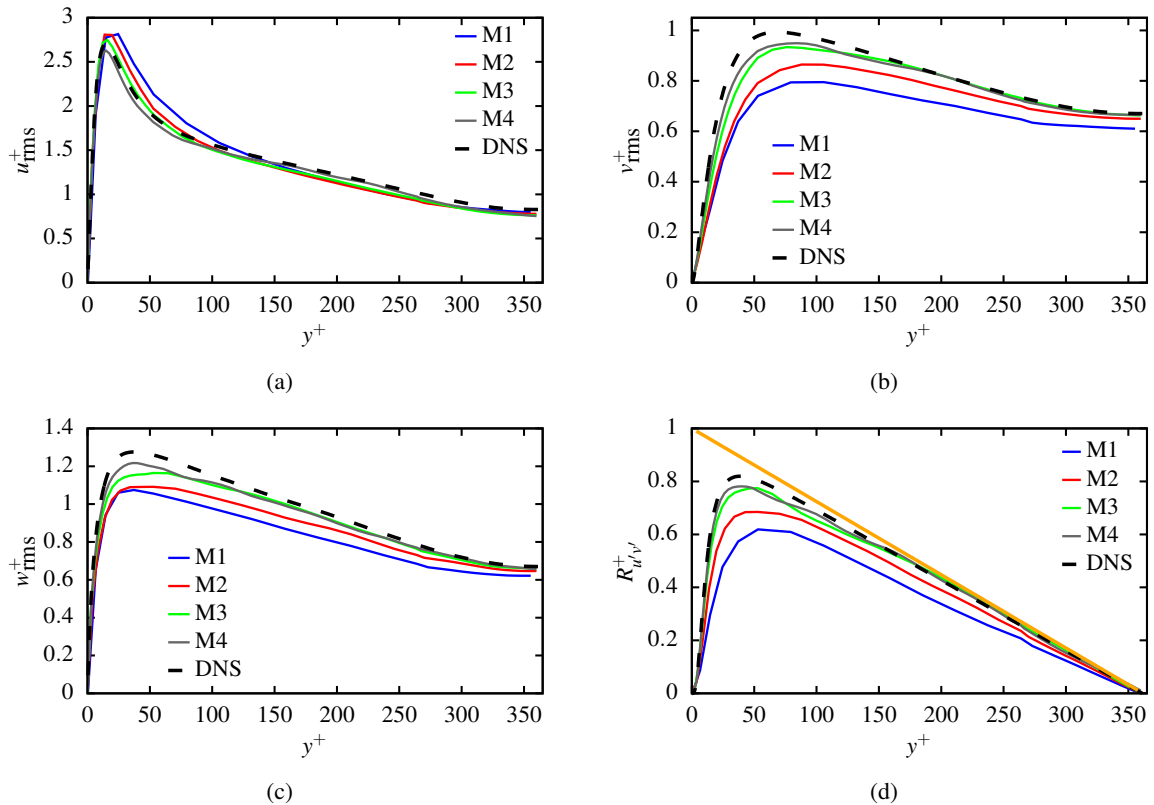


FIG. 3: Comparison of LES-WALE and DNS data for (a) axial, u_{rms}^+ , (b) wall-normal, v_{rms}^+ , and (c) azimuthal, w_{rms}^+ , turbulence intensities, and (d) turbulent shear stresses, $R_{u'v'}^+$. The DNS data at $Re_\tau = 361$ are shown in dashed black line. The thin diagonal line represents the total shear stress, with the difference between this line and the data indicating the viscous shear stress attributed to the mean flow.

tion, the results from the LES gradually approach the DNS results, as shown in Figs. 2 and 3 of Sec. IV A. The reason for this is that as Δ decreases k_{sgs} and v_{sgs} also decrease approximately as Δ^2 . Since the objective of this sensitivity study is to examine the influence of the subgrid model, it is

advisable to use the coarser meshes. The coarser meshes will emphasize the differences between the subgrid models more effectively. On finer meshes, we will not be able to detect any noticeable differences between the models. Therefore, to facilitate an effective comparison, mesh M2 has been se-

TABLE II: Computed global flow parameters for different grid resolutions. $Re_\tau = u_\tau^0 D / (2\nu)$, and $Re_\tau^{ap} = u_\tau D / (2\nu)$ are the a priori and a posteriori estimates of Re_τ , respectively. u_τ^0 and u_τ are the a priori and a posteriori estimates of the friction velocity, respectively. $f_{D_{\text{num}}}$ and $f_{D_{\text{exp}}}$ are numerical estimation and target value of the Darcy friction coefficient, respectively. $f_{D_{\text{relErr}}}$ the relative error in the numerical computation of f_D .

Mesh	Re_b	Re_τ	Re_τ^{ap}	$f_{D_{\text{num}}}$	$f_{D_{\text{exp}}}$	$f_{D_{\text{relErr}}}$
M1	11,700	361	322	0.0242	0.0296	18%
M2	11,700	361	343	0.0279	0.0296	6%
M3	11,700	361	357	0.0298	0.0296	1%
M4	11,700	361	360	0.0303	0.0296	2.4%
DNS	11,700	361	361	0.03040	0.0296	2.7%

lected.

Table III presents a priori and a posteriori estimates of Re_τ , estimates of $f_{D_{\text{num}}}$, $f_{D_{\text{exp}}}$, and $f_{D_{\text{relErr}}}$ for each subgrid model. It is noted that, across all cases, the simulated f_D values are slightly underpredicted compared to targeted values. However, no discernible trend linking f_D with subgrid models is evident, with negligible differences in f_D values among the various models. Although additional refinement near the wall could potentially enhance results, the impact on different models remains uncertain. Nevertheless, in line with the LES philosophy, such *improvement* would come at the expense of increased computational requirements – an outcome undesirable in the context of this subgrid model comparison.

To assess predictive abilities in both near-wall and outer regions, we calculate mean velocity and mean velocity-defect profiles normalized in wall units. Fig. 4 (a) displays mean velocity profiles in wall units, while Fig. 4 (b) shows mean velocity-defect profiles in the outer region for different subgrid models. Analyzing Fig. 4, all subgrid models exhibit distinct behaviors, clustering based on their predictive capabilities. Near the wall, LES-WALE and LES-LDKM accurately predict mean velocity profiles, while LES-DSEM is also accurate but slightly less so. In contrast, LES-SMG and LES-OEEVM slightly underpredict near-wall mean flow but show reasonable agreement with DNS data and other models in the core flow region.

Our computational models yield slightly lower Re_τ than El Khoury *et al.* [7]. This results in slight overestimates in mean velocity profiles when normalized using inner units compared to DNS data [7]. In Fig. 4 (b), showing mean velocity-defect profiles, there is a slight underestimation compared to DNS values. This occurs as we used the theoretical value of u_τ as a normalization parameter instead of the actual value measured in each simulation, see Fig. 14 in Appendix A. For $y/R > 0.65$, all curves collapse onto DNS results. Additionally, all mean velocity profiles exhibit a log-law behavior above the buffer layer, i.e., $y^+ \geq 30$ (see the orange solid line in Fig. 4 (a)). In our results, the logarithmic representation of turbulent profiles shows a universal behavior across subgrid models, with values $1/\kappa = 2.5$ and $B^+ = 5.2$, proposed and accepted for various canonical flows.

RMS velocity fluctuation values are shown in Figs. 5 (a-c). LES-SMG and LES-OEEVM underpredict peak values and overpredict their locations compared to LES-WALE,

LES-LDKM, LES-DSEM, and DNS. LES-WALE, LES-LDKM, and LES-DSEM accurately predict peak locations but overestimate the values. This aligns with observations in other channel flow studies where u_{rms}^+ tends to be overpredicted in LES compared to DNS [68]. For v_{rms}^+ and w_{rms}^+ , all subgrid models exhibit excellent qualitative behavior compared to DNS, as shown in Figs. 5 (b-c). However, quantitatively, all subgrid models underpredict the fluctuation values. LES-OEEVM and LES-SMG are highly diffusive near the wall and fail to predict peak values accurately. In contrast, LES-LDKM and LES-WALE behave closely to DNS but with some underprediction. Surprisingly, LES-DSEM emerges as the most accurate candidate when compared to DNS. Both profiles of velocity fluctuations (cyan data in Figs. 5 (b-c)) show good agreement with DNS due to their anisotropic nature, albeit with slight underprediction. This may be related to fixed values of coefficients c_m and c_e in the kinetic energy distribution equation (Eq. (4)) in the DSEM subgrid model. While dynamically computing these coefficients could improve predictions, such enhancements are beyond the scope of this paper.

$R_{u'v'}^+$ profiles in Fig. 5 (d) show similar behavior to DNS for LES-WALE, LES-LDKM, and LES-DSEM models. In the viscous wall region ($y^+ < 15$) and outer region ($y^+ > 50$), $R_{u'v'}^+$ becomes linear. Quantitatively, LES-WALE and LES-LDKM reproduce DNS tendencies, including a peak at $y^+ \simeq 30$ and semi-linear behavior in the outer region. Both subgrid models accurately predict the peak location, albeit with a slight underestimation of its value. Surprisingly, LES-DSEM closely agrees with DNS compared to LES-WALE and LES-LDKM. In contrast, LES-SMG and LES-OEEVM tend to overpredict the peak location while underpredicting the peak value, consistent with rms values of velocity fluctuations in Figs. 5 (a-c).

C. Investigation of fully-developed turbulent flows for Re_τ ranging from 361 to 2,000

The analysis thus far suggests that the DSEM, WALE, and LDKM subgrid models accurately predict flow behavior. Therefore, we proceed with the WALE model for further exploration at high Re_τ values. We choose not to use LDKM and DSEM, as our earlier observation suggests similar pre-

TABLE III: Computed global flow parameters for different subgrid models. $Re_\tau = u_\tau^0 D / (2\nu)$, and $Re_\tau^{ap} = u_\tau D / (2\nu)$ are the a priori and a posteriori estimates of Re_τ , respectively. u_τ^0 and u_τ are the a priori and a posteriori estimates of the friction velocity, respectively. $f_{D_{num}}$ and $f_{D_{exp}}$ are numerical estimation and target value of the Darcy friction coefficient, respectively. $f_{D_{relErr}}$ the relative error in the numerical computation of f_D .

Subgrid model	Mesh	Re_b	Re_τ	Re_τ^{ap}	$f_{D_{num}}$	$f_{D_{exp}}$	$f_{D_{relErr}}$
OEEVM	M2	11,700	361	344	0.0276	0.0296	7%
SMG	M2	11,700	361	342	0.0274	0.0296	7%
WALE	M2	11,700	361	345	0.0279	0.0296	6%
LDKM	M2	11,700	361	345	0.0278	0.0296	6%
DSEM	M2	11,700	361	374	0.0327	0.0296	10%
DNS		11,700	361	361	0.03040	0.0296	2.7%

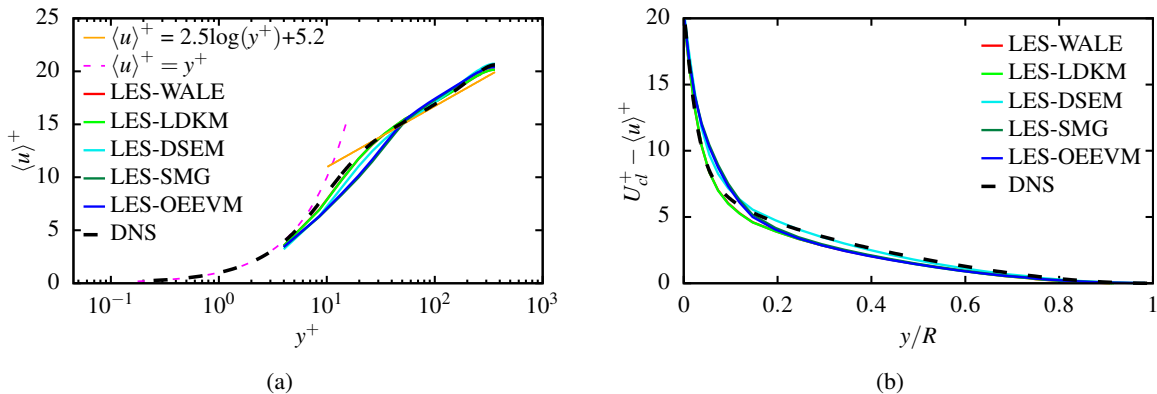


FIG. 4: (a) Mean velocity profiles and (b) mean velocity-defect profiles for $Re_\tau = 361$ and five different subgrid models, normalized by u_τ^0 which is a priori estimate of the friction velocity. U_{cl}^+ is the normalized centerline velocity. The dashed black line presents DNS data from El Khoury *et al.* [7] and the dashed pink and solid orange lines in Fig. 4 (a) represent the universal behavior of the turbulent velocity profile.

diction capabilities among WALE, LDKM, and DSEM, simplifying the computational process. This simplifies the computational process by selecting one model. Results are compared against previously reported DNS results [7, 23] for four different Re_τ values: 361, 550, 1,000, and 2,000. In all simulations, Re_τ values are initially undefined and computed a posteriori, with Re_b values taken from El Khoury *et al.* [7] and Pirozzoli *et al.* [23]. To explore near-wall-modeled LES behavior under coarse grid conditions and high Re_τ , we choose the coarse M2 grid as the base grid for $Re_\tau = 361$, where approximately 85% of turbulent Reynolds shear stresses and turbulent kinetic energy are resolved. Following Pope [73], this implies using a grid marginally acceptable for LES in the high Re study, expecting errors to be at least as high as for $Re_\tau = 361$ or possibly higher.

1. Mesh refinement based on Taylor scaling

To resolve a relatively similar amount of turbulent Reynolds shear stresses and turbulent kinetic energy for higher Re_τ , we estimate the integral, Taylor, and Kolmogorov scales using conventional approximations. The

integral length scale, l_I , is set as the pipe diameter, i.e., $l_I = D$. The Taylor scale, λ , an intermediate length scale in the inertial subrange, is estimated as $\lambda = \sqrt{(15\nu/\epsilon)u_{rms}}$ [74]. Here, $u_{rms} = \sqrt{(u'^2 + v'^2 + w'^2)}/3$ is the root mean square of the velocity fluctuations. The Kolmogorov scale, η , dissipation subrange, is estimated as $\eta = (\nu^3/\epsilon)^{1/4}$ [75]. Combining the expression for the Kolmogorov scale with the dissipation rate, $\epsilon \simeq k^{3/2}/l_I$, where $k = \frac{3}{2}u_{rms}^2$, yields $\eta/l_I = C(u_{rms}l_I/\nu)^{-3/4} = CRe_l^{-3/4}$, with $C \simeq 0.86$ as a constant and Re_l as the integral scale Re number. The value of u_{rms} , can be approximated using the turbulent intensity, I , as $u_{rms} = IU_b$, where $I = 10\%$ for high turbulence intensity applications. The grid resolution needed to resolve a relatively similar amount of the turbulent Reynolds shear stresses and the turbulent kinetic energy as at $Re_\tau = 361$ for higher Re_τ values is computed from the expression of λ/l_I and provided in Table IV.

Table IV presents a priori and a posteriori Re_τ estimations. The chosen Re_b value is deemed adequate. As expected, Re_τ is underpredicted in all simulations (Table IV). However, the earlier grid resolution analysis suggests significant improvement with refinement, indicating eventual convergence

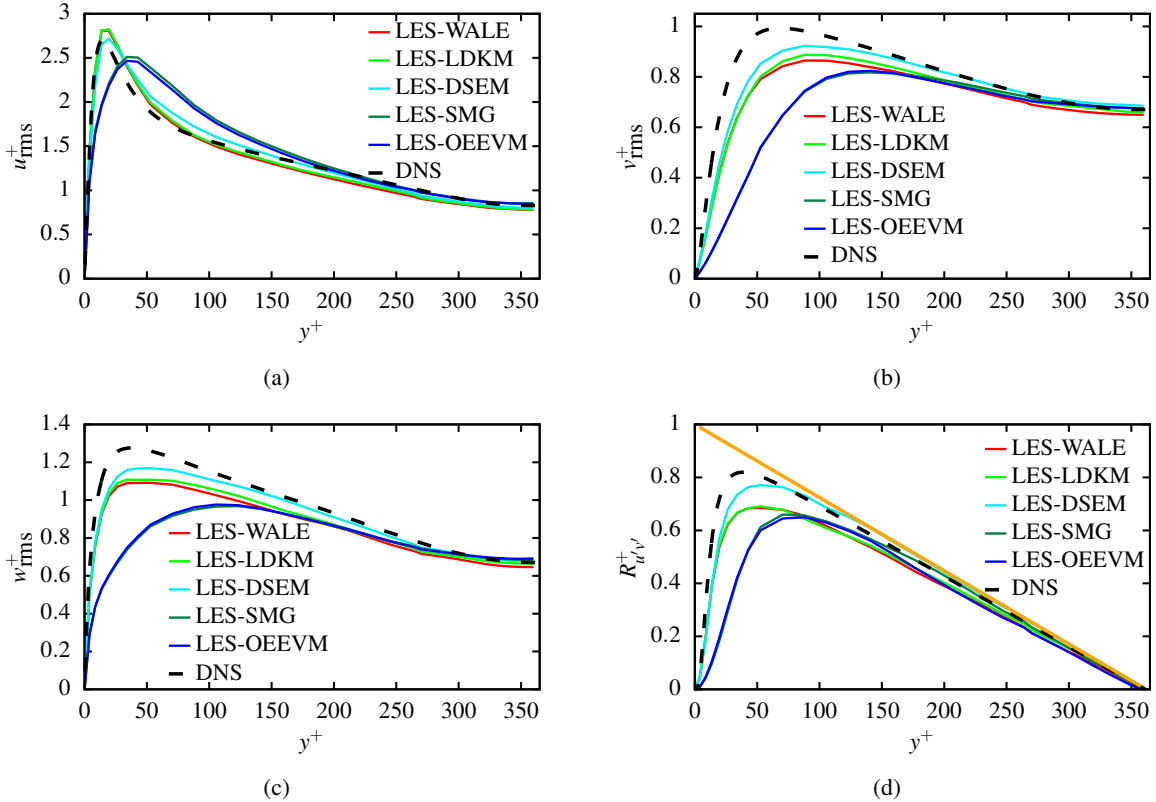


FIG. 5: Comparison of (a) axial, u_{rms}^+ , (b) wall-normal, v_{rms}^+ , and (c) azimuthal, w_{rms}^+ , turbulence intensities; (d) turbulent Reynolds shear stress, $R_{u'v'}^+$, with DNS data (dashed lines) as functions of y^+ , at $Re_\tau = 361$, for different subgrid models. The thin diagonal line represents the total shear stress, with the difference between this line and the data indicating the viscous shear stress attributed to the mean flow.

TABLE IV: Computed global flow parameters for different turbulent Re_τ . $Re_\tau = u_\tau^0 D / (2\nu)$, and $Re_\tau^{ap} = u_\tau D / (2\nu)$ are the a priori and a posteriori estimates of Re_τ , respectively. u_τ^0 and u_τ are the a priori and a posteriori estimates of the friction velocity, respectively. $f_{D_{\text{num}}}$ and $f_{D_{\text{exp}}}$ are numerical estimation and target value of the Darcy friction coefficient, respectively. $f_{D_{\text{relErr}}}$ the relative error in the numerical computation of f_D .

Grids	Re_b	Mesh total size	Re_τ	Re_τ^{ap}	$f_{D_{\text{num}}}$	$f_{D_{\text{exp}}}$	$f_{D_{\text{relErr}}}$
G1	11,700	0.5M cells	361	345	0.0279	0.0296	5%
G2	19,000	1.0M cells	550	517	0.0237	0.0262	9%
G3	37,700	2.3M cells	1,000	928	0.0194	0.0223	13%
G4	82,500	6.5M cells	2,000	1,780	0.0149	0.0187	20%

to Re_τ . Numerical estimations of $f_{D_{\text{num}}}$ for various turbulent Re_τ , along with $f_{D_{\text{exp}}}$ values, are in Table IV. Deviations of approximately 5-20% from expected results are observed.

In Fig. 6 (a), mean velocity profiles from LES-WALE are compared to DNS data for various Re_τ values. A generally good agreement is observed, especially in the inner layer and overlap regions, with data gradually converging to a logarithmic distribution. Fig. 6 (b) shows profiles of streamwise turbulent velocity fluctuations normalized by u_τ^2 in relation to Re_τ . For low Re_τ , results match DNS profiles, but as Re_τ increases, differences between LES-WALE and DNS become more pronounced. Specifically, LES-WALE

consistently overpredicts the peak value of u_{rms}^+ for each Re_τ , intensifying with higher Re_τ . Conversely, in the outer region, LES-WALE tends to underestimate velocity fluctuations, more noticeable with increasing Re_τ . Meshes based on Taylor scaling do not capture fluctuations' overshoot in the outer region observed in DNS. Results from Berrouk *et al.*[46] and Ferrer *et al.*[47] also show discrepancies with DNS data. This could be due to our grid resolution and seems inherent in LES subgrid models, as seen in our previous grid resolution study, even for grid M3. A more detailed investigation with advanced subgrid models like DSEM is recommended, although beyond the scope of this study.

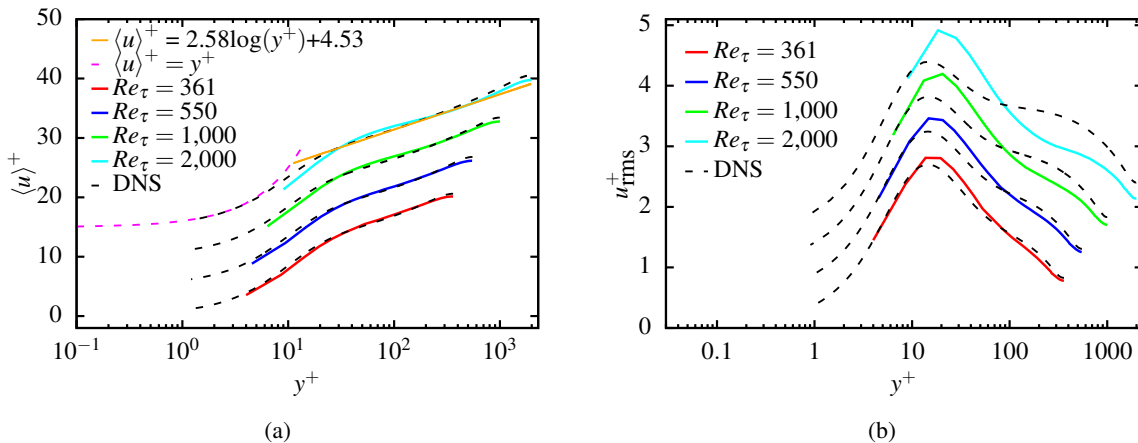


FIG. 6: Comparison of (a) $\langle u \rangle^+$ and (b) u_{rms}^+ , as functions of y^+ for different values of Re_τ and the WALE subgrid model. u_{rms}^+ profiles are plotted with an offset of $\Delta \langle \cdot \rangle^+ = 1$ for clarity. In all figures, the DNS data are represented in dashed black lines.

2. Optimizing Mesh: Directional Refinement for Improved Results

To address the mesh resolution issue related to large-scale fluctuations, we revisited our meshing strategy, initially based on Taylor’s scale. We conducted simulations at $Re_\tau = 1000$ for several new generated grids (G31, G32, G33, G34) with decreasing mesh spacing in all directions. Similar meshes were generated for $Re_\tau = 361, 550, 2,000$. Additional details on the grids are available in Table. V. Results for M1-M4 are already presented in Sec. IV A.

Figure 7 displays mean turbulent shear stress and rms streamwise velocities for various meshes at $Re_\tau = 1000$, along with DNS data for comparison. G32, G33, and G34 simulations show collapsed profiles for turbulent shear stress, while G3 and G31, using coarser resolution based on Taylor’s scale, underestimate the results. This suggests grid convergence is achieved for $\Delta y_{\text{wall}}^+ \sim 3, \Delta z^+ \sim 15, \Delta x^+ \sim 30$. However, for similar resolution, Fig. 7 (b) shows that rms velocity fluctuations are not collapsed. Good agreement with DNS data is only observed with G34. Comparing profiles for G3, G31, G32, and G33, it is observed that to accurately capture small-scale fluctuations, especially overshoots in the outer region, in the presence of wall models, Δy^+ values can be relaxed, but Δx^+ and Δz^+ values play a significant role and must be strictly constrained. A trend can even be established between the peak rms velocity and the grid resolution: the former improves when the mesh resolution is respected as follows: $\Delta z^+ \leq 10, \Delta x^+ = 20 - 25$. Moreover, the G34 mesh resolution is determined by the Kolmogorov scales, specifically the grid points utilized in LES-WALE, denoted as $N_{LES} \approx (2.25 \cdot Re_\tau)^{9/4}$. It is worth noting that the factor 2.25 differs from the one employed in DNS studies, which is 3 [76].

Before doing further quantitative analysis, we show the evolution of the vortical structures for different Re_τ values in Fig. 8. Vortices, identified using the λ_2 -criterion and plotted for $\lambda_2/\lambda_{2\text{max}} = -0.01$, appear densely along the pipe

from the wall upto the wall-normal location $y/R \simeq 0.5$. Notably, with increasing Re_τ , fluctuations and resolved vortical structures become finer and more amplified. Streaks become discernible in the near-wall cylindrical shells, arranged in a cross-stream pattern. Regardless of turbulent Re , low-speed streaks (deep blue color, approximately the size of the pipe radius) align with large-scale ejections, while high-speed streaks (red-yellow color, of same size as low-speed streaks) correspond to substantial inflow from the core flow. Smaller streaks appear, corresponding to ejection and sweep events in the buffer layer. The flow organization on at least two length scales is apparent, with the separation increasing as Re_τ values escalate.

In Fig. 9 (a), we present mean velocity profiles computed with LES-WALE for $Re_\tau = 361, 550, 1,000$, and $2,000$ using new meshes M4, G21, G34, and G41. A good agreement is observed between LES-WALE and DNS, particularly in the inner layer and overlap regions, with the data gradually converging to a logarithmic distribution. This log-law is visually fitted as $\langle u \rangle^+ = (1/\kappa)\log(y^+) + B$, with coefficients $\kappa = 0.387$ and $B = 4.53$ from Pirozzoli *et al.* [23]. The results closely aligns with the estimates from direct fitting of mean velocity profiles in pipe flows [77], yielding $\langle u \rangle^+ = (1/\kappa)\log(y^+) + B$, with $\kappa = 0.391$ and $B = 4.34$. Not much difference is obtained compared to results from coarser meshes, shown in Fig. 6 (a).

Figure 10 (a) provides insights into the turbulent shear stress distribution for varying Re_τ values. As Re_τ increases, the shear stress profiles flatten, with the peak value rising toward unity, and its position shifting further from the wall. This well-established behavior [69] is characterized by the asymptotic relationship that accounts for the position of the turbulent shear stress peak, y_p^+ [78],

$$y_p^+ \simeq \sqrt{\frac{Re_\tau}{\kappa}}. \quad (8)$$

The precision of Eq. (8), with $\kappa = 0.387$, is notably accurate starting from $Re_\tau \simeq 1,000$ onwards, indicating the onset

TABLE V: Parameters of the new grid used for the grid convergence study; mesh spacings are given in wall units; Δx^+ , Δz^+ : mesh spacings in the streamwise and azimuthal directions; Δy_{wall}^+ , Δy_{center}^+ : mesh spacings in the wall normal direction at the wall and at the center of the channel.

Grids	Re_τ	Mesh total size	Δx^+	Δy_{wall}^+	Δy_{center}^+	Δz^+
M1	361	0.13M cells	40	5	8	24
M2/G1	361	0.5M cells	28	3	6	16
M3	361	1.5M cells	20	3	4	12
M4	361	5M cells	13	2	3	4
G2	550	1M cells	32	4	6	19
G21	550	8M cells	17	2	3	10
G3	1000	2.3M cells	44	6	9	26
G31	1000	2.8M cells	42	1e-2	8	24
G32	1000	8M cells	44	7e-2	4	11
G33	1000	15M cells	28	3	5	15
G34	1000	36M cells	19	2	4	11
G4	2000	6.5M cells	59	7	12	35
G41	2000	218M cells	19	2	4	10

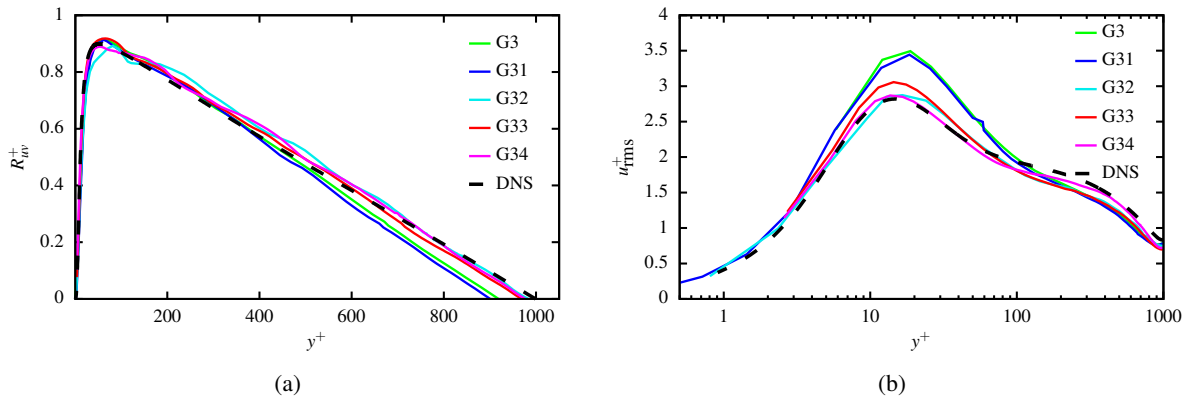


FIG. 7: (a) Turbulent shear stresses (R_{uv}^+) and (b) axial turbulent velocity fluctuations (u_{rms}^+) on a semi-logarithmic scale, are shown as a function of y^+ at $Re_\tau = 1,000$ for the WALE subgrid model. In all subfigures, the DNS data are represented in dashed black lines.

of a near-logarithmic layer [79]. In our simulations, the predicted peak position, y_p^+ , closely aligns with expected values for $Re_\tau = 1,000$ and $2,000$, with deviations of approximately 5%. However, for $Re_\tau < 1,000$, the predictions deviate significantly from the asymptotic relation, showing deviations of roughly 27%.

Based on the proposed criteria we have further looked upon the velocity fluctuations results for $Re_\tau = 361, 550, 1000$ and $2,000$ in Fig. 10 (b-d). Compared with the results obtained using Taylor scaling (Fig. 6 (b)), the present results matches with the DNS, as shown in Fig. 10. Slight discrepancies between DNS results and LES at $Re_\tau = 2,000$ can still be observed; nevertheless, both the primary peaks and the secondary overshoot region are well captured in comparison to existing literature [46, 47]. Unlike previous results, the mesh requirement for $Re_\tau = 2000$ is $\sim 220M$ cells and increases tremendously with Re_τ . Therefore, we restrict this study to $Re_\tau = 2000$.

Single point statistics

To quantitatively depict near-wall regions at different Re_τ , we utilize quadrant analysis for streamwise and wall-normal velocity fluctuations. Quadrant analysis divides the (u', v') plane into four quadrants (Q_1, Q_2, Q_3, Q_4) based on sign combinations of velocity fluctuations. Specifically, Q_1 corresponds to positive values of both u' and v' , Q_2 represents $u' < 0, v' > 0$, Q_3 indicates $u' < 0, v' < 0$, and Q_4 corresponds to $u' > 0, v' < 0$. Ejection-like events occur in Q_2 , while sweep-like events are in Q_4 . Quadrant analysis provides insights into the dynamics of near-wall streaks, initially observed by Kline *et al.* [80] and further explored by Corino & Brodkey [81] and Wallace *et al.* [82]. Willmarth & Lu [83] computed quadrant contributions to the total shear stress, highlighting the importance of ejection and sweep events in the production of turbulent Reynolds shear stress. The shear stress plays a crucial role in turbulence

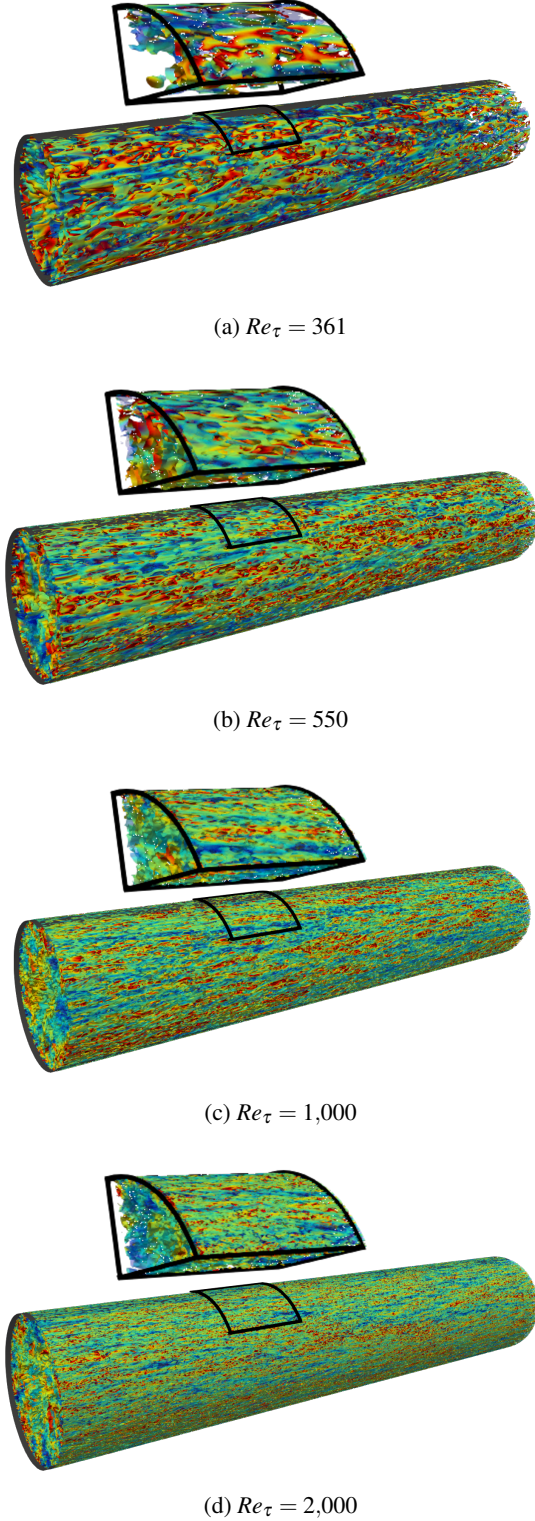


FIG. 8: Visualization of vortical structures using the λ_2 -criterion, color-coded by streamwise velocity fluctuations, u' (a) $Re_\tau = 361$ (M4 mesh), (b) $Re_\tau = 550$ (G21 mesh), (c) $Re_\tau = 1,000$ (G34 mesh), and (d) $Re_\tau = 2,000$ (G41 mesh). Color scale ranges from -0.3 (blue) to 0.3 (red) and zoomed-in views are provided for clarity.

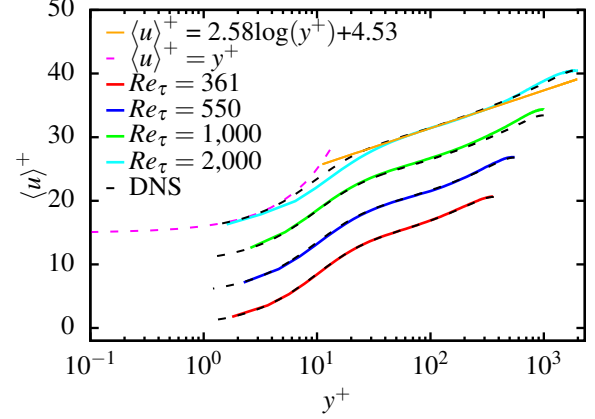


FIG. 9: Comparison of $\langle u \rangle^+$ as function of y^+ for different values of Re_τ and the WALE subgrid model. u_{rms}^+ profiles are plotted with an offset of $\Delta \langle \cdot \rangle^+ = 5$ for clarity. DNS data is shown with dashed black lines. The dashed pink and solid orange lines depict the universal behavior of the turbulent streamwise velocity profile.

dynamics, appearing in the LES equation and the turbulent kinetic energy equation's production term, P_{ij} , multiplied by the mean shear stress.

$$P_{ij}^k = -\langle u'_i u'_j \rangle \frac{\partial \langle u_i \rangle}{\partial x_j}. \quad (9)$$

Fig. 11 shows contour plots of the joint probability density function (JPDF) of velocity fluctuations, $P(u', v')$, normalized by their local rms values, $\sigma_{u'}$ and $\sigma_{v'}$. These plots are at $y^+ = 3\sqrt{Re_\tau}$ for four Re_τ values. The JPDF iso-contours have an elliptical shape, mainly spanning quadrants Q₂ and Q₄, with the maximum value in Q₄, indicating a higher frequency of $\{u'v'(t) < 0\}$ events, particularly with more extreme values in Q₂ (ejections). Normalized PDFs are also displayed on the top (u') and right (v') corners in each plot. Fig. 12 presents PDFs of streamwise and wall-normal velocity fluctuations, $P(u')$ and $P(v')$, at various distances from the wall for different Re_τ . These PDFs concern fluctuations relative to the mean and are normalized by the root-mean-square value. In the near-wall region (Fig. 12 (a)), the distribution of streamwise velocity fluctuations, u' , deviates significantly from a Gaussian shape, indicating intermittency with more intense and intermittent high-speed streaks close to the wall. This behavior contributes to the positive skewness observed in experiments [84] and DNS [85]. The PDFs of wall-normal fluctuations, v' , (Fig. 12 (c)), are weakly asymmetric, favoring descents over ascents. In the outer region of the pipe ($y^+ = 150$), the PDF shapes approach a Gaussian distribution (Fig. 12 (b), (d)), indicating that Re_τ has minimal impact on the overall dominance of ejection- and sweep-like events.

Anisotropy of turbulence for different Reynolds numbers

The anisotropy of unsteady turbulent flows is important

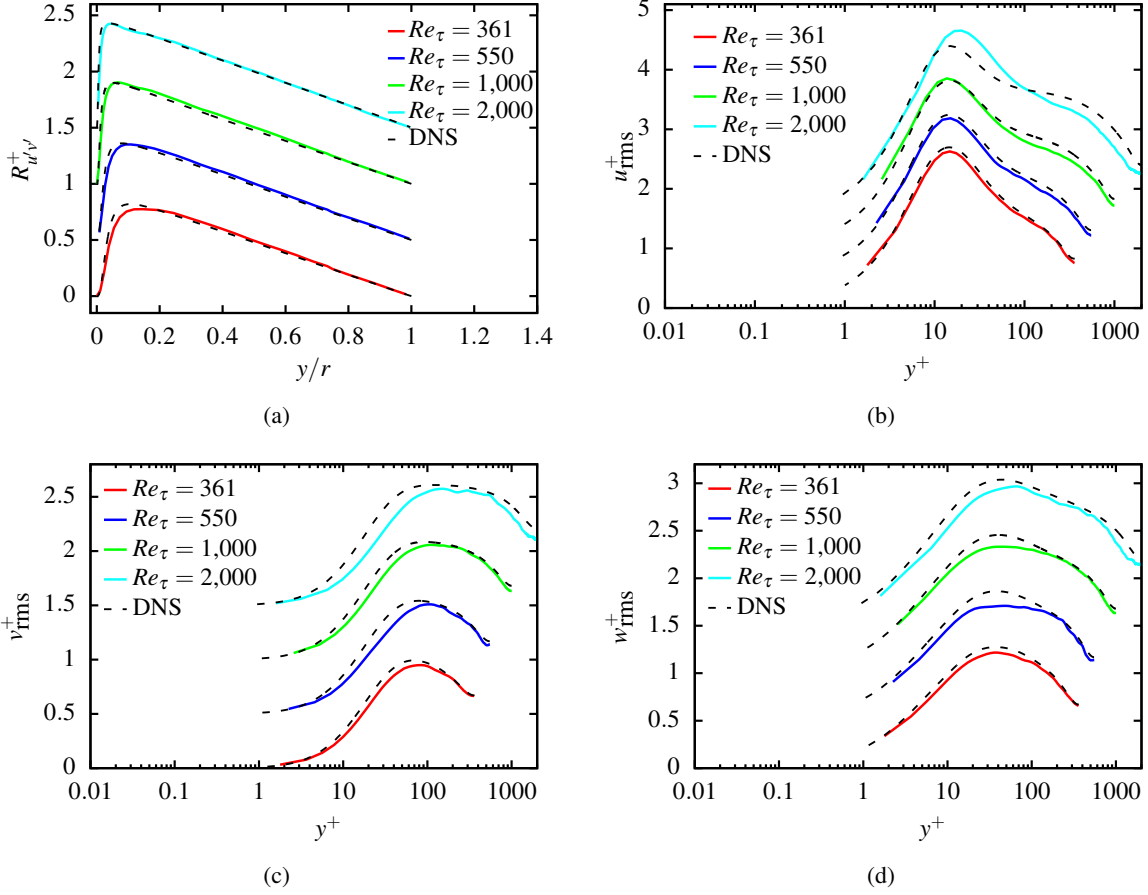


FIG. 10: (a) Turbulent shear stresses, $R_{u'v'}^+$ and turbulent velocity fluctuations (b) u_{rms}^+ , (c) v_{rms}^+ , and (d) w_{rms}^+ , corresponding to different values of Re_τ and the WALE subgrid model, are shown as a function of y^+ and offset by $\Delta \langle \cdot \rangle^+ = 1$ for clarity. In all subfigures, the DNS data are represented in dashed black lines.

characteristics of turbulence. Turbulence anisotropy is represented by the degree of departure from isotropic turbulence. Accurate numerical simulations require precise predictions of anisotropy for various flow situations such as those encountered in atmospheric science and engineering design, which can be quantified using the second (II_b) and third (III_b) invariants of the normalized anisotropy tensor, b_{ij} , given by

$$b_{ij} = \frac{\langle u'_i u'_j \rangle}{\langle u'_k u'_k \rangle} - \frac{1}{3} \delta_{ij}. \quad (10)$$

The state of anisotropy can then be characterized with the two variables η and ξ defined as

$$\eta^2 = -\frac{1}{3} II_b \quad (11)$$

and

$$\xi^3 = -\frac{1}{2} III_b. \quad (12)$$

Reynolds stress tensor states are confined within the Lumley triangle, defined in the (ξ, η) plane, with different realizable states characterized by the invariants of the normalized

anisotropy tensor, b_{ij} . Details on these states can be found in [86]. Anisotropy maps in Fig. 13 depict variations for four Re_τ values across y^+ . These maps utilize all somain cells, and post-processed values of η and ξ are represented with a color map of y^+ , indicating the likelihood of specific turbulent states. Near the wall, turbulence is highly two-dimensional (dominated by $u'u'$ and $w'w'$ fluctuations), transitioning toward a one-dimensional, one-component state as $u'u'$ peaks around $y^+ \simeq 8$, as highlighted in the inset of Fig. 13. As y^+ increases, data points move toward the origin, aligning along the axisymmetric state, signifying an approach to isotropy. These findings align well with Pope's analysis [75] of DNS data from Kim *et al.* [66], where two-component turbulence was identified near the wall ($y^+ < 5$), transitioning to axisymmetric expansion in the channel's remaining portion. The anisotropy maps exhibit a universal behavior across different Re_τ values.

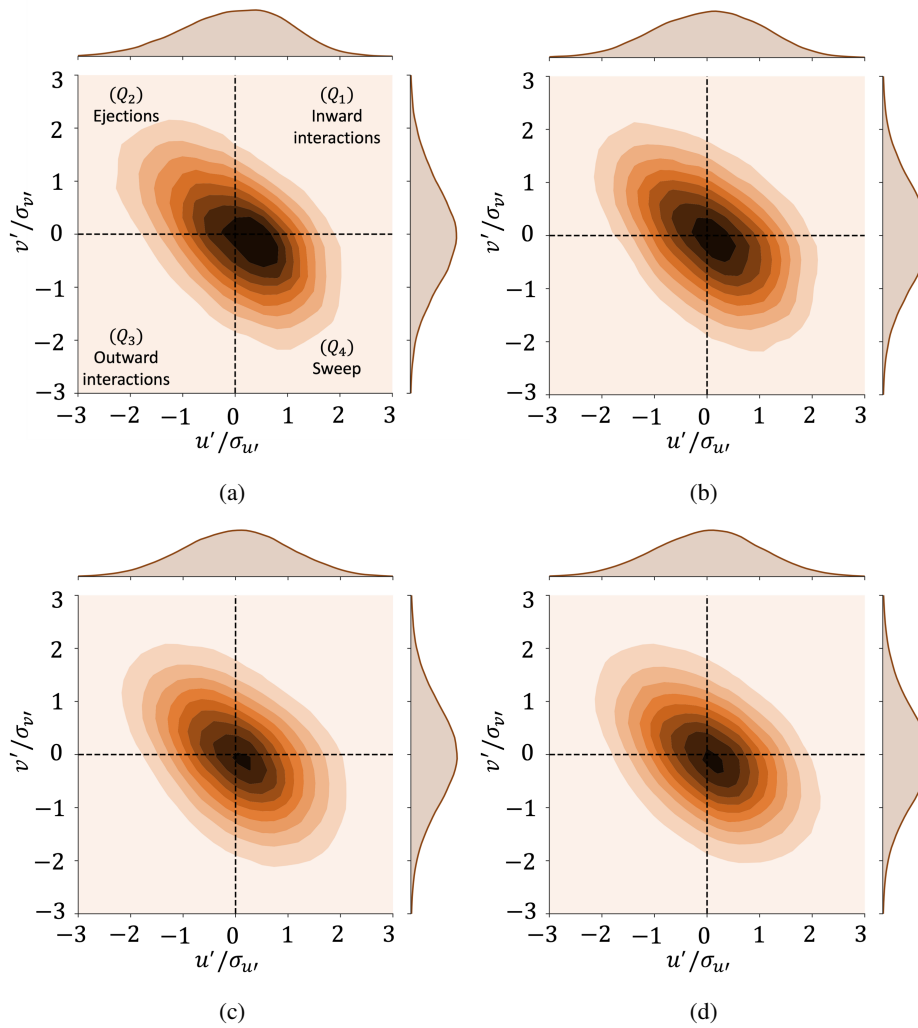


FIG. 11: Quadrant plots illustrate axial, u' , and wall-normal, v' , velocity fluctuations normalized by their root-mean-squares, $\sigma_{v'}$, for different turbulent Re_τ and for the WALE subgrid model, at $y^+ = 3\sqrt{Re_\tau}$: (a) $Re_\tau = 361$, (b) $Re_\tau = 550$, (c) $Re_\tau = 1,000$, and (d) $Re_\tau = 2,000$. Each plot includes PDFs of $u'/\sigma_{u'}$ and $v'/\sigma_{v'}$ on the top and right corners, respectively.

V. CONCLUSIONS

The present work assesses the prediction capabilities of wall-modeled Large Eddy Simulations (LES) at moderate-to-high Reynolds numbers and in the limit of coarse meshes, in the OpenFOAM framework. Initially, results for a turbulent pipe flow at $Re_\tau = 361$ were compared against DNS data available in the literature. The simulation results obtained using the WALE subgrid model showed excellent qualitative and quantitative prediction accuracy when compared to DNS data; nonetheless, with slight underprediction of all turbulence characteristics. We further assessed the accuracy of the WALE subgrid model by performing a grid resolution study on four different grids (M1, M2, M3, and M4, where M1 is the coarsest grid, and M4 is the finest grid). The results showed a gradual increase in accuracy of zeroth-, first-, and second-order critical turbulence statistics with grid resolution. However, as a trade-off between numerical accuracy

and computational wall clock time, we decided to proceed with a rather coarse M2 grid for further detailed investigations.

Based on the grid resolution study, we performed LES for five different subgrid models: the Wall-Adapting Local Eddy viscosity model (WALE), the Smagorinsky model (SMG), the One-Equation Eddy Viscosity Model (OEEVM), the Localized Dynamic Kinetic energy Model (LDKM), and the Differential Stress Equation Model (DSEM) on grid M2. The results obtained demonstrated that WALE, LDKM, and DSEM were able to reproduce the main and most critical characteristics of turbulent flows, featuring regions of high strain rates and large-scale vortices, with higher accuracy than OEEVM and SMG, both quantitatively and qualitatively, in comparison to DNS data from the literature. Observing the flow statistics, it could be evidenced that the estimates of the mean flow profiles and turbulent Reynolds shear stresses were consistent for the three subgrid models

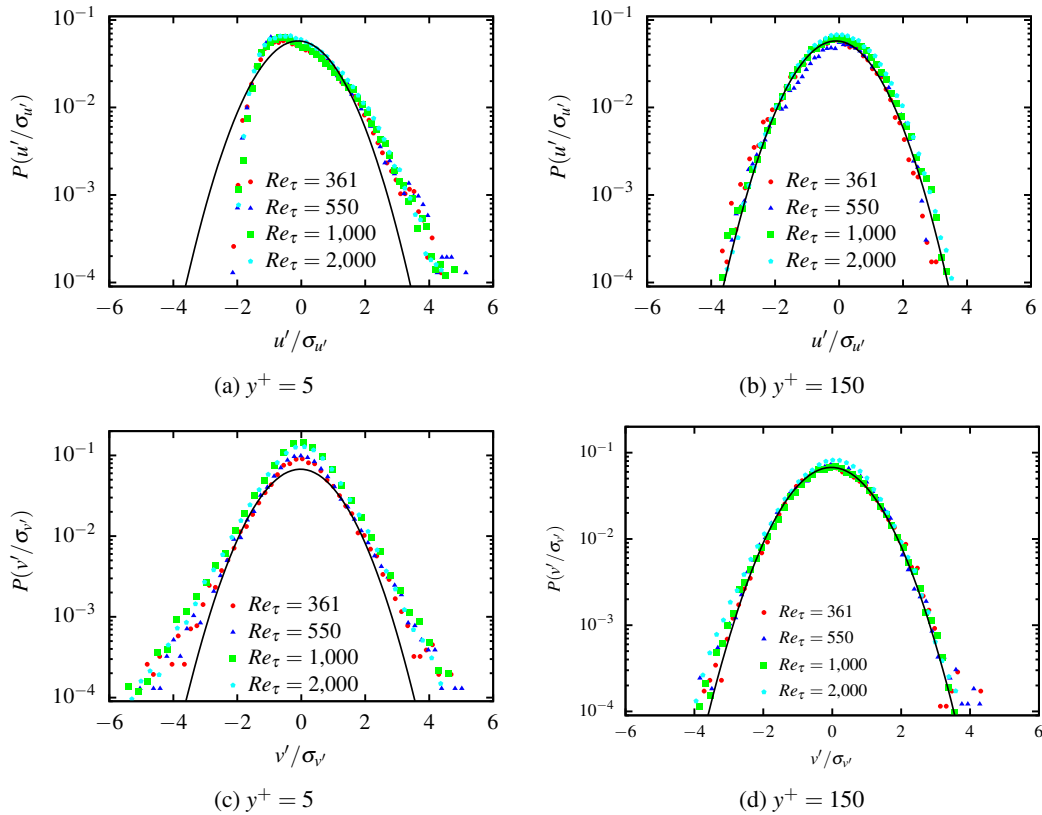


FIG. 12: Probability Distribution Functions (PDF) of streamwise velocity fluctuations, $u'/\sigma_{u'}$ (a) close to the wall ($y^+ = 5$), (b) in the outer region ($y^+ = 150$), and wall-normal velocity fluctuations, $v'/\sigma_{v'}$ (c) close to the wall ($y^+ = 5$), (d) in the outer region ($y^+ = 150$), for different values of Re_τ and the WALE subgrid model. The PDF are normalized by their rms values, $\sigma_{u'}$.

(WALE, LDKM, and DSEM). Still, DSEM showed a better overall performance in predicting the near-wall and outer region statistics, particularly for v_{rms}^+ and w_{rms}^+ , possibly due to its anisotropic assumption. The DSEM model still slightly overpredicts all the flow statistical quantities in the core region. This is possibly due to the fact that the physical constants of this model are not computed dynamically, as opposed to the LDKM model whose accuracy is then improved. However, the differences between the results obtained with WALE and LDKM were insignificant, and both models provided highly accurate profiles of mean flow and turbulent Reynolds shear stresses.

Additionally, to strengthen our analysis and assess the prediction capabilities of subgrid models, we performed LES utilizing WALE for four moderate turbulent $Re_\tau = 361, 550, 1,000$, and $2,000$, and compared them against DNS data available in the literature. To stress on the potential of the near-wall-modeled LES in the limit of a coarse grid and high Re_τ , in the present analysis the M2 grid is chosen as a base grid for $Re_\tau = 361$. The grid has then been refined to resolve roughly the same amount of turbulent shear stresses and turbulent kinetic energy for $Re_\tau = 550$ to $2,000$. Estimating the zeroth- and first-order statistics showed that WALE gives reasonable results compared to DNS upto $Re_\tau = 550$ and deviate slowly with a further increase of Re_τ . In the present

wall-modeled LES another outcome that surprised us is the failure of the wall models for high Re_τ . Firstly, the Reynolds stress tensors exhibited reasonable agreement with DNS data in the outer region for all values of Re_τ . However, they also revealed a dramatic deviation from the DNS data in the subviscous layer region at all values of Re_τ . Secondly, velocity fluctuation profiles show strong deviations from DNS, even for moderate Re_τ . Surprisingly, the secondary-peak region is poorly captured. This observation is peculiar and raises questions about the validity of the scaling based on Taylor and integral scales ($\lambda/l_l \propto Re^{-1/2}$) used to obtain relatively similar meshes for different values of Re_τ . Based on the considered scaling, similar resolution was expected for different Re_τ values, but the results showed the opposite both in the wall region (a smaller number of mesh nodes when moving from $Re_\tau = 1,000$ to $2,000$) and outer region (secondary peak is not captured). The results from Berrouk *et al.* and Ferrer *et al.* also demonstrate discrepancies with DNS data, both regarding the primary peak and the secondary overshoot. This observation suggests that LES with WALE requires greater refinement in the wall-normal direction than the one used in the current work to more accurately anticipate the behavior of the smallest-scale motions. This indicates the need for a different scaling factor to resolve a relatively similar amount of turbulent shear stress with increasing Re . Upon

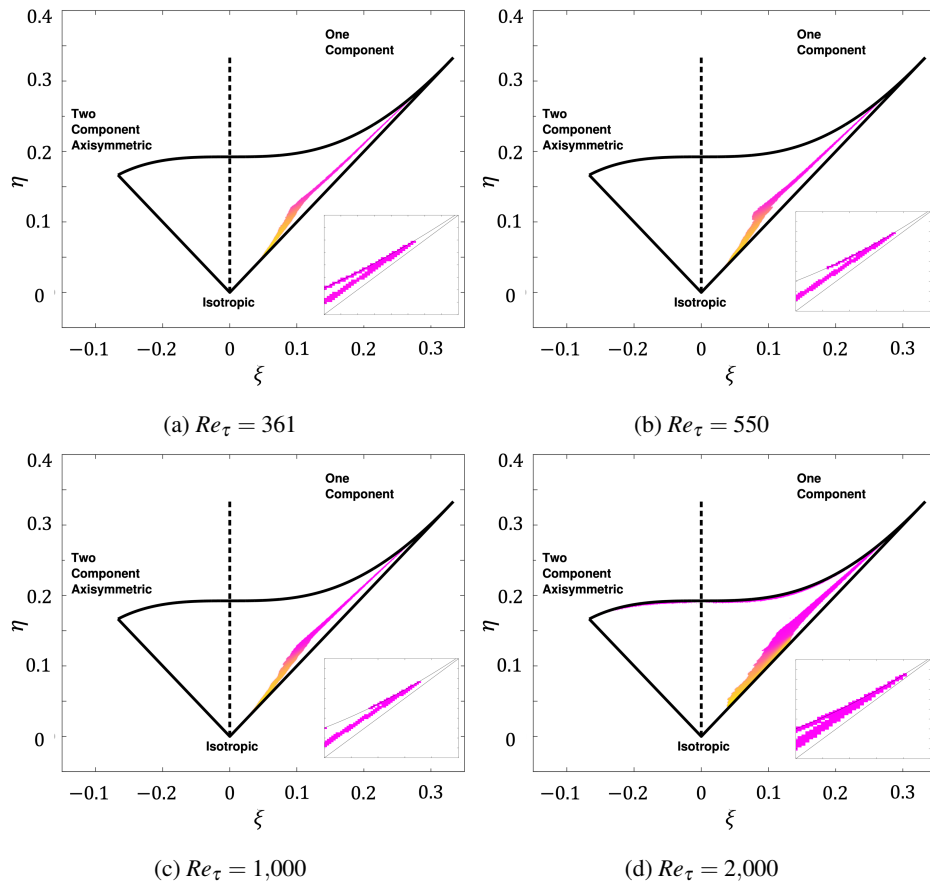


FIG. 13: Anisotropy-invariant mapping of turbulence from present LES-WALE data at (a) $Re_\tau = 361$, (b) $Re_\tau = 550$, (c) $Re_\tau = 1,000$, and (d) $Re_\tau = 2,000$. Data points for each subgrid model are based on all cells in the domain and are colored with normalized wall distance values, y^+ . The color map varies from pink to yellow. Insets in all subfigures show the same zoom of the one-component turbulence area.

further investigation of grid convergence using Kolmogorov scaling, it was found that to accurately capture second-order statistics, particularly secondary overshoots in fluctuations, it is necessary to utilize $\Delta x^+ \leq 20 - 25$ and $\Delta z^+ \leq 10$. This leads to an actual number of grid points required for well-resolved LES of pipe flow, denoted as N_{LES} , at approximately $(2.25 \cdot Re_\tau)^{9/4}$. The coefficient differs from DNS, which is 3. While the computational savings compared to DNS are extremely significant, they amount to at least 30%.

To conclude, our findings suggest that the scaling strategy we have explored in this paper is not effective, and we advise against others attempting to replicate this approach. Rather, we recommend a different methodology that involves a direct measurement of the resolution using appropriate criteria such as modeled kinetic energy and grid variations that ensure comparable resolutions across different Re_τ . Although this approach can be time-consuming and challenging, it is essential for achieving relatively similar resolutions across different Reynolds numbers. Therefore, we suggest either the use of grid spacing constraint proposed above or the use of simulation methods that replace the filter width with a modeled length scale and include the modeled kinetic en-

ergy for resolution calculations. By adopting these methods, one can ensure a more accurate and reliable resolution for the simulations in various physical and engineering applications.

ACKNOWLEDGEMENT

The authors greatly appreciate the financial support provided by Vinnova under project number "2020-04529". Computer time was provided by the Swedish National Infrastructure for Computing (SNIC), partially funded by the Swedish Research Council through grant agreement no. 2018-05973.

AUTHOR DECLARATIONS

Conflict of interest

The authors have no conflicts of interest to disclose.

Data availability

The data that support the findings of this study are available from the corresponding author upon reasonable request.

Appendix A: Mean velocity-defect profile

Figure 14 shows mean velocity-defect velocity profiles in the outer region for various subgrid models. All results are normalized with u_τ . The difference between Fig. 4(a) and Fig. 14 lies in the normalization. In Fig. 4(a), all results are normalized by u_τ^0 . For the definition, refer to Table. III.

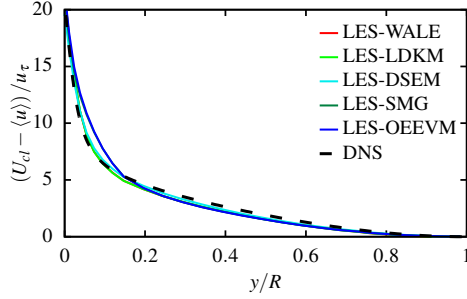


FIG. 14: Mean velocity-defect profiles for $Re_\tau = 361$ and five different subgrid models, normalized by u_τ . The value of u_τ is estimated from the simulations. U_{cl}^+ is the normalized centerline velocity. The dashed black line presents DNS data from El Khoury *et al.* [7].

Appendix B: Autocorrelations functions

The correlations of the velocity fluctuations in each direction are typically characterized by means of statistical tools. Notably, a standard tool to assess the relationship between the velocity fluctuations in the streamwise and wall-normal directions is the coefficient of correlation. Our measurements allow us to quantitatively assess the correlations of velocity fluctuations in time and space. The temporal correlation functions of the velocity fluctuation components, defined as

$$C_{i'}(T) = \frac{\langle i'(t+T)i'(t) \rangle_t}{\langle [i'(t)]^2 \rangle_t}, \quad i = u, v, \quad (\text{B1})$$

where the brackets indicate the time average and T is the time interval between two consecutive sample points.

Similarly, the spatial cross-correlation function of each velocity component is defined as

$$C_{i'}(X) = \frac{\langle i'(x+X)i'(x) \rangle_x}{\langle [i'(x)]^2 \rangle_x}, \quad i = u, v, \quad (\text{B2})$$

where the brackets indicate an average over the x -direction and X is the distance between two points along the given direction.

The correlations of the two-point velocity fluctuations computed from Eq. (B1) in the temporal and spatial domains as functions of the turbulent Re_τ are shown in Fig. 15 (a-c) and 15 (d-f), respectively. It should be noted that data for cross-correlation analysis in the x -direction are extracted at $y = R$ and averaged using 100 line probes. The profiles indicate that the chosen duration of simulation is long enough to capture all the relevant turbulent structures, since they fluctuate around the zero value for all components. The corresponding correlation times, computed as $t_{i'} = \int_0^{T_{\max}} C_{i'}(T) dT$ are reported in Table VI, where T_{\max} is the duration of the largest time increment.

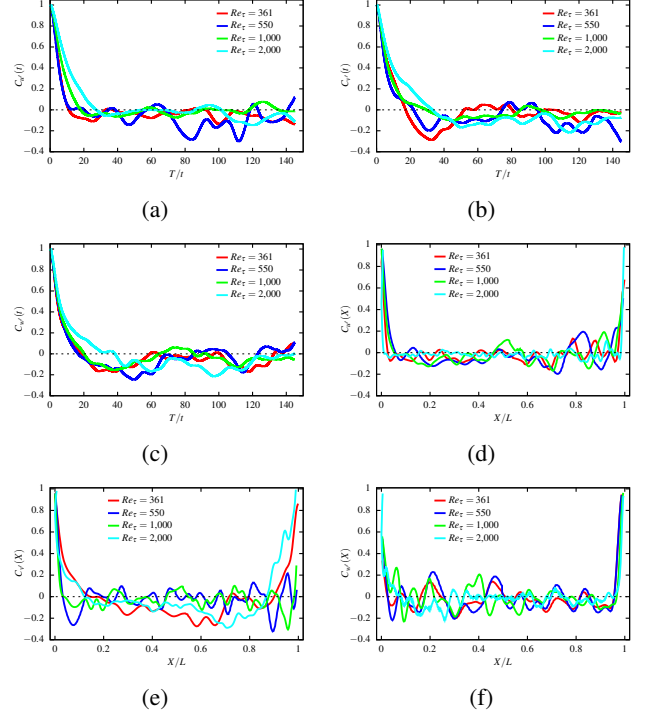


FIG. 15: Normalized one-dimensional temporal and spatial autocorrelation functions of (a), (d) axial velocity fluctuations, u' , (b), (e) wall-normal velocity fluctuations, v' , and (c), (f) azimuthal velocity fluctuations, w' , for different values of Re_τ .

TABLE VI: Correlation times and lengths in the streamwise direction of axial, u' , wall-normal, v' , and azimuthal, w' , velocity fluctuation components. The correlation times are computed as $t_{i'} = \int_0^{T_{\max}} C_{i'}(T)dT$, while the correlation lengths are deduced from the zero-crossing lengths of the corresponding autocorrelation functions, $C_{i'}(X)$.

Re_τ	$T_{u'}/t$	$T_{v'}/t$	$T_{w'}/t$	$l_{u'}/L$	$l_{v'}/L$	$l_{w'}/L$
361	11.092	17.338	19.318	0.034	0.188	0.046
550	20.379	22.176	16.622	0.058	0.033	0.026
1,000	18.256	20.099	20.134	0.052	0.041	0.077
2,000	27.731	33.448	38.431	0.012	0.122	0.079

- ¹R. B. Stull and C. D. Ahrens, *Meteorology for scientists and engineers* (Brooks/Cole, 2000).
- ²S. A. Thorpe, *The turbulent ocean* (Cambridge University Press, 2005).
- ³I. Marusic, B. J. McKeon, P. A. Monkewitz, H. M. Nagib, A. J. Smits, and K. R. Sreenivasan, “Wall-bounded turbulent flows at high Reynolds numbers: recent advances and key issues,” *Phys. Fluids* **22**, 065103 (2010).
- ⁴P. Manneville, “Transition to turbulence in wall-bounded flows: Where do we stand?” *Mech. Eng. Rev.*, 15–00684 (2016).
- ⁵A. J. Smits, B. J. McKeon, and I. Marusic, “High-Reynolds number wall turbulence,” *Annu. Rev. Fluid Mech.* **43**, 353–375 (2011).
- ⁶J. P. Monty, *Developments in smooth wall turbulent duct flows*, Ph.D. thesis, University of Melbourne, Department of Mechanical and Manufacturing Engineering (2005).
- ⁷G. K. El Khoury, P. Schlatter, A. Noorani, P. F. Fischer, G. Brethouwer, and A. V. Johansson, “Direct numerical simulation of turbulent pipe flow at moderately high Reynolds numbers,” *Flow Turbul. Combust.* **91**, 475–495 (2013).
- ⁸J. Jiménez, “Cascades in wall-bounded turbulence,” *Annu. Rev. Fluid Mech.* **44**, 27–45 (2012).
- ⁹F. H. Clauser, “The turbulent boundary layer,” *Adv. Appl. Mech.* **4**, 1–51 (1956).
- ¹⁰D. Coles, “Computation of turbulent boundary layers,” in *AFOSR-IFP Stanford Conference, CA* (Citeseer, 1969).
- ¹¹R. Örlü, T. Fiorini, A. Segalini, G. Bellani, A. Talamelli, and P. H. Alfredsson, “Reynolds stress scaling in pipe flow turbulence—first results from clopoe,” *Philos. Trans. Royal Soc. A* **375**, 20160187 (2017).
- ¹²J. G. M. Eggels, F. Unger, M. H. Weiss, J. Westerweel, R. J. Adrian, R. Friedrich, and F. T. M. Nieuwstadt, “Fully developed turbulent pipe flow: a comparison between direct numerical simulation and experiment,” *J. Fluid Mech.* **268**, 175–210 (1994).
- ¹³R. A. Antonia, M. Teitel, J. Kim, and L. W. B. Browne, “Low-Reynolds-number effects in a fully developed turbulent channel flow,” *J. Fluid Mech.* **236**, 579–605 (1992).
- ¹⁴J. M. J. Den Toonder and F. T. M. Nieuwstadt, “Reynolds number effects in a turbulent pipe flow for low to moderate Re ,” *Phys. Fluids* **9**, 3398–3409 (1997).
- ¹⁵C. Wagner, T. J. Hüttl, and R. Friedrich, “Low-Reynolds-number effects derived from direct numerical simulations of turbulent pipe flow,” *Comp. & Fluids* **30**, 581–590 (2001).
- ¹⁶C. Peng, N. Geneva, Z. Guo, and L. P. Wang, “Direct numerical simulation of turbulent pipe flow using the lattice boltzmann method,” *J. Comput. Phys.* **357**, 16–42 (2018).
- ¹⁷X. Wu and P. Moin, “A direct numerical simulation study on the mean velocity characteristics in turbulent pipe flow,” *J. Fluid Mech.* **608**, 81–112 (2008).
- ¹⁸C. Chin, A. S. H. Ooi, I. Marusic, and H. M. Blackburn, “The influence of pipe length on turbulence statistics computed from direct numerical simulation data,” *Phys. Fluids* **22**, 115107 (2010).
- ¹⁹J. Klewicki, C. Chin, H. M. Blackburn, A. Ooi, and I. Marusic, “Emergence of the four layer dynamical regime in turbulent pipe flow,” *Phys. Fluids* **24**, 045107 (2012).
- ²⁰J. H. Lee and H. J. Sung, “Comparison of very-large-scale motions of turbulent pipe and boundary layer simulations,” *Phys. Fluids* **25**, 045103 (2013).
- ²¹C. Chin, J. P. Monty, and A. Ooi, “Reynolds number effects in DNS of pipe flow and comparison with channels and boundary layers,” *Int. J. Heat Fluid Flow* **45**, 33–40 (2014).
- ²²A. Junsun, L. Jae Hwa, L. Jin, K. Ji-hoon, and S. Hyung Jin, “Direct numerical simulation of a 30r long turbulent pipe flow at $re_\tau = 3008$,” *Phys. Fluids* **27**, 065110 (2015).
- ²³S. Pirozzoli, J. Romero, M. Fatica, R. Verzicco, and P. Orlandi, “One-point statistics for turbulent pipe flow up to $Re_\tau \approx 6000$,” *J. Fluid Mech.* **926**, A28 (2021).
- ²⁴J. Yao, S. Rezaeiravesh, P. Schlatter, and F. Hussain, “Direct numerical simulation of turbulent pipe flow up to $Re_\tau = 5200$,” (2022), 10.48550/ARXIV.2207.06289.
- ²⁵M. Guala, S. E. Hommema, and R. J. Adrian, “Large-scale and very-large-scale motions in turbulent pipe flow,” *J. Fluid Mech.* **554**, 521–542 (2006).
- ²⁶J. P. Monty, J. A. Stewart, R. C. Williams, and M. S. Chong, “Large-scale features in turbulent pipe and channel flows,” *J. Fluid Mech.* **589**, 147–156 (2007).
- ²⁷M. V. Zagarola and A. J. Smits, “Mean-flow scaling of turbulent pipe flow,” *J. Fluid Mech.* **373**, 33–79 (1998).
- ²⁸N. Furuichi, E. Kusano, Y. Wada, and Y. Tsuji, “Experimental study for turbulent pipe flow at high Reynolds number using LDV-Turbulent intensity profile and influence of measurement volume,” *Bull. Am. Phys. Soc.* **64**, G11.002 (2019).
- ²⁹G. N. Coleman and R. D. Sandberg, “A primer on direct numerical simulation of turbulence - methods, procedures and guidelines,” Project Report (2010).
- ³⁰V. Yakhot and K. R. Sreenivasan, “Anomalous scaling of structure functions and dynamic constraints on turbulence simulations,” *J. Stat. Phys.* **121**, 823–841 (2005).
- ³¹P. Sagaut, *Large eddy simulation for incompressible flows: an introduction* (Springer Science & Business Media, 2006).
- ³²A. Misra and D. I. Pullin, “A vortex-based subgrid stress model for large-eddy simulation,” *Phys. Fluids* **9**, 2443–2454 (1997).
- ³³H. Pitsch, “Large eddy simulation of turbulent combustion,” Tech. Rep. 1 (Leland Stanford Junior University, 2006).
- ³⁴G. Matheou, A. M. Bonanos, C. Pantano, and P. E. Dimotakis, “Large-eddy simulation of mixing in a recirculating shear flow,” *J. Fluid Mech.* **646**, 375–414 (2010).
- ³⁵A. Ferrante, G. Matheou, and P. E. Dimotakis, “LES of an inclined sonic jet into a turbulent crossflow at Mach 3.6,” *J. Turb. N2* (2011).
- ³⁶U. Piomelli and E. Balaras, “Wall-layer models for large-eddy simulations,” *Annu. Rev. Fluid Mech.* **34**, 349–374 (2002).
- ³⁷J. A. Templeton, G. Medic, and G. Kalitzin, “An eddy-viscosity based near-wall treatment for coarse grid large-eddy simulation,” *Phys. Fluids* **17**, 105101 (2005).
- ³⁸U. Piomelli, “Wall-layer models for large-eddy simulations,” *Prog. Aero. Sci.* **44**, 437–446 (2008).
- ³⁹J. A. Templeton, M. Wang, and P. Moin, “A predictive wall model for large-eddy simulation based on optimal control techniques,” *Phys. Fluids* **20**, 065104 (2008).
- ⁴⁰D. Chung and D. I. Pullin, “Large-eddy simulation and wall modelling of

- turbulent channel flow," *J. Fluid Mech.* **631**, 281–309 (2009).
- ⁴¹C. Fureby, N. Alin, N. Wikström, S. Menon, N. Svanstedt, and L. Persson, "Large eddy simulation of high-Reynolds-number wall bounded flows," *AIAA journal* **42**, 457–468 (2004).
- ⁴²N. J. Georgiadis, D. P. Rizzetta, and C. Fureby, "Large-eddy simulation: current capabilities, recommended practices, and future research," *AIAA journal* **48**, 1772–1784 (2010).
- ⁴³J. Larsson, S. Kawai, J. Bodart, and I. Bermejo-Moreno, "Large eddy simulation with modeled wall-stress: recent progress and future directions," *Mech. Eng. Rev.* **3**, 15–00418 (2016).
- ⁴⁴C. Fureby, "High fidelity numerical simulations of ship and sub-marine hydrodynamics," in *MARINE VII: proceedings of the VII International Conference on Computational Methods in Marine Engineering (CIMNE, 2017)* pp. 23–47.
- ⁴⁵A. J. Smits and I. Marusic, "Wall-bounded turbulence," *Phys. Today* **66**, 25–30 (2013).
- ⁴⁶A. S. Berrouk, D. Laurence, J. J. Riley, and D. E. Stock, "Stochastic modelling of inertial particle dispersion by subgrid motion for LES of high Reynolds number pipe flow," *J. Turb.*, N50 (2007).
- ⁴⁷E. Ferrer, N. Saito, H. M. Blackburn, and D. I. Pullin, "High-Reynolds-number wall-modelled large eddy simulations of turbulent pipe flows using explicit and implicit subgrid stress treatments within a spectral element solver," *Comp. & Fluids* **191**, 104239 (2019).
- ⁴⁸F. Nicoud and F. Ducros, "Subgrid-scale stress modelling based on the square of the velocity gradient tensor," *Flow Turbul. Combust.* **62**, 183–200 (1999).
- ⁴⁹J. Smagorinsky, "General circulation experiments with the primitive equations: I. The basic experiment," *Mon. Weather Rev.* **91**, 99–164 (1963).
- ⁵⁰U. Schumann, "Subgrid scale model for finite difference simulations of turbulent flows in plane channels and annuli," *J. Comput. Phys.* **18**, 376–404 (1975).
- ⁵¹W. W. Kim and S. Menon, "A new dynamic one-equation subgrid-scale model for large eddy simulations," in *33rd Aerospace Sciences Meeting and Exhibit* (1995) p. 356.
- ⁵²W. W. Kim and S. Menon, "Application of the localized dynamic subgrid-scale model to turbulent wall-bounded flows," in *35th Aerospace Sciences Meeting and Exhibit* (1997) p. 210.
- ⁵³J. W. Deardorff, "The Use of Subgrid Transport Equations in a Three-Dimensional Model of Atmospheric Turbulence," *J. Fluids Eng.* **95**, 429–438 (1973).
- ⁵⁴C. G. Speziale, "Galilean invariance of subgrid-scale stress models in the large-eddy simulation of turbulence," *J. Fluid Mech.* **156**, 55–62 (1985).
- ⁵⁵B. Vreman, B. Geurts, and H. Kuerten, "Realizability conditions for the turbulent stress tensor in large-eddy simulation," *J. Fluid Mech.* **278**, 351–362 (1994).
- ⁵⁶C. Fureby and G. Tabor, "Mathematical and physical constraints on large-eddy simulations," *Theor. Comput. Fluid Dyn.* **9**, 85–102 (1997).
- ⁵⁷Y. Li, L. Chevillard, G. Eyink, and C. Meneveau, "Matrix exponential-based closures for the turbulent subgrid-scale stress tensor," *Phys. Rev. E* **79**, 016305 (2009).
- ⁵⁸D. K. Lilly, "On the application of the eddy viscosity concept in the inertial sub-range of turbulence," NCAR manuscript **123** (1966), <http://dx.doi.org/10.5065/D67H1GGQ>.
- ⁵⁹C. Fureby, G. Tabor, H. G. Weller, and A. D. Gosman, "Differential subgrid stress models in large eddy simulations," *Phys. Fluids* **9**, 3578–3580 (1997).
- ⁶⁰J. C. Butcher, *Numerical methods for ordinary differential equations* (John Wiley & Sons, 2016).
- ⁶¹H. G. Weller, G. Tabor, H. Jasak, and C. Fureby, "A tensorial approach to computational continuum mechanics using object-oriented techniques," *Comp. Phys.* **12**, 620–631 (1998).
- ⁶²G. H. Golub and C. F. Van Loan, *Matrix Computations*, Johns Hopkins Studies in the Mathematical Sciences (Johns Hopkins University Press, 2013).
- ⁶³W. H. Press, S. A. Teukolsky, W. T. Vetterling, and B. P. Flannery, *Numerical recipes 3rd edition: The art of scientific computing* (Cambridge university press, 2007).
- ⁶⁴B. W. Kernighan and D. M. Ritchie, *The m4 macro processor* (Bell Laboratories Murray Hill, NJ, 1977).
- ⁶⁵F. Jeong, J. and Hussain, "On the identification of a vortex," *J. Fluid Mech.* **285**, 69–94 (1995).
- ⁶⁶J. Kim, P. Moin, and R. Moser, "Turbulence statistics in fully developed channel flow at low Reynolds number," *J. Fluid Mech.* **177**, 133–166 (1987).
- ⁶⁷P. Moin and J. Kim, "Numerical investigation of turbulent channel flow," *J. Fluid Mech.* **118**, 341–377 (1982).
- ⁶⁸S. T. Bose, P. Moin, and D. You, "Grid-independent large-eddy simulation using explicit filtering," *Phys. Fluids* **22**, 105103 (2010).
- ⁶⁹M. Lee and R. D. Moser, "Direct numerical simulation of turbulent channel flow up to $Re_\tau = 5200$," *J. Fluid Mech.* **774**, 395–415 (2015).
- ⁷⁰D. B. De Graaff and J. K. Eaton, "Reynolds-number scaling of the flat-plate turbulent boundary layer," *J. Fluid Mech.* **422**, 319–346 (2000).
- ⁷¹M. H. Chaudhry, *Applied hydraulic transients* (Springer, 1979).
- ⁷²L. F. Moody, "Friction factors for pipe flow," *Trans. Asme* **66**, 671–684 (1944).
- ⁷³S. B. Pope, "Ten questions concerning the large-eddy simulation of turbulent flows," *New J. Phys.* **6**, 35 (2004).
- ⁷⁴G. I. Taylor, "Statistical theory of turbulence-II," *Proc. R. Soc. London. Ser. A* **151**, 444–454 (1935).
- ⁷⁵S. B. Pope, *Turbulent flows* (Cambridge university press, 2000).
- ⁷⁶D. C. Wilcox, *Turbulence modeling for CFD*, Vol. 2 (DCW industries La Canada, CA, 1998).
- ⁷⁷I. Marusic, J. P. Monty, M. Hultmark, and A. J. Smits, "On the logarithmic region in wall turbulence," *J. Fluid Mech.* **716**, R3 (2013).
- ⁷⁸N. Afzal, "Fully developed turbulent flow in a pipe: an intermediate layer," *Ing. Arch.* **52**, 355–377 (1982).
- ⁷⁹C. Chin, J. Philip, J. Klewicki, A. Ooi, and I. Marusic, "Reynolds-number-dependent turbulent inertia and onset of log region in pipe flows," *J. Fluid Mech.* **757**, 747–769 (2014).
- ⁸⁰S. J. Kline, W. C. Reynolds, F. A. Schraub, and P. W. Runstadler, "The structure of turbulent boundary layers," *J. Fluid Mech.* **30**, 741–773 (1967).
- ⁸¹E. R. Corino and R. S. Brodkey, "A visual investigation of the wall region in turbulent flow," *J. Fluid Mech.* **37**, 1–30 (1969).
- ⁸²J. M. Wallace, H. Eckelmann, and R. S. Brodkey, "The wall region in turbulent shear flow," *J. Fluid Mech.* **54**, 39–48 (1972).
- ⁸³W. W. Willmarth and S. S. Lu, "Structure of the Reynolds stress near the wall," *J. Fluid Mech.* **55**, 65–92 (1972).
- ⁸⁴T. Fiorini, *Turbulent Pipe Flow - High Resolution Measurements in CIC-LoPE*, Ph.D. thesis, Università di Bologna, Scuola di Ingegneria e Architettura (2017).
- ⁸⁵L. Redjem-Saad, M. Ould-Rouiss, and G. Lauriat, "Direct numerical simulation of turbulent heat transfer in pipe flows: Effect of Prandtl number," *Int. J. Heat Fluid Flow* **28**, 847–861 (2007).
- ⁸⁶J. L. Lumley and G. R. Newman, "The return to isotropy of homogeneous turbulence," *J. Fluid Mech.* **82**, 161–178 (1977).